COMPARISON OF THE MULTI-ANODE PMTS WITH THE OLD HF PMTS BY STUDYING THE COLLISION DATA

by

Yavuz Öz

B.S, Physics, Boğaziçi University, 2010

Submitted to the Institute for Graduate Studies in
Science and Engineering in partial fulfillment of
the requirements for the degree of
Master of Science

Graduate Program in Physics

Boğaziçi University

2013

ACKNOWLEDGEMENTS

I would like to express my deepest gratitude to Prof. Erhan Gülmez for his patience, guidance and assistance he has shown as my thesis supervisor and graduate advisor. I would also like to thank my co-supervisor Associate Professor Taylan Yetkin for his patience and insight, who guided my studies with his experience and comprehensive knowledge and dedicated a lot of his time from his busy schedule.

I would like to thank my dear family for their support and understanding. I would also like to express my deeply-felt gratitude to my beloved girlfriend Elif Özülkü; her love, support and devotion has given me purpose and strength throughout my undergraduate and graduate career.

I am grateful to Bora Işıldak, Serhat Iştın and Cemile Ezer for their professional and personal support at both CERN and Boğaziçi University.

Finally, I would like to thank the Boğaziçi University Research Fund for their support provided through the grant #6653 (Project #12B03P2).

ABSTRACT

COMPARISON OF THE MULTI-ANODE PMTS WITH THE OLD HF PMTS BY STUDYING THE COLLISION DATA

The Hadron Forward (HF) calorimeter of the CMS detector improves jet detection and missing transverse energy resolution in the high pseudorapidity range. HF employs photomultiplier tubes (PMT) that measure the Čerenkov light emitted by shower products in quartz fibers. Stray muons that hit a PMT window create high energy events that are difficult to reject. To alleviate this problem, the PMTs installed in the CMS will be replaced with those of better performance. From among various candidate PMTs, quad-anode Hamamatsu R7600U-200-M4 were chosen to replace the single-anode Hamamatsu R7525HA PMTs. The quad-anode PMTs offer the possibility to reject window events at the hardware level; muons hitting the window are localized to a single anode, while real events illuminate all four anodes. In 2011, eight such PMTs were installed in the readout boxes corresponding to the coordinates $i\phi = 67$, $i\eta = 29, 30, 31, 32$, which get very few hits on account of their location. The purpose of this thesis is to compare the response of the old and new PMTs to window hits using pulseshape analysis. It is shown that the new PMTs offer significantly better noise performance, simply by virtue of their thinner windows.

ÖZET

HF'TEKİ YENİ ÇOK ANOTLU VE ESKİ TEK ANOTLU FOTOTÜPLERİN ÇARPIŞMA VERİLERİ İNCELENEREK KARŞILAŞTIRILMASI

CMS dedektöründeki İleri Hadronik Kalorimetresi (HF), yüksek psödorapidite bölgesinde jet ölçümlerini ve proton demetine dik yöndeki kayıp enerjinin belirlenmesini iyileştirir. HF dedektöründeki fotoçoğaltıcı tüpler, kuartz fiberlerden gelen Čerenkov ışığını ölçer. Fototüplerin camlarına çarpan ortalığa saçılmış fondaki müonlar, ayıklaması güç olan yüksek enerjili ölçümlere sebep olur. Bu problemi azaltmak için CMS HF dedektöründeki fototüpler daha iyi performans veren modelleriyle değiştirilecektir. Aday fototüpler arasından, eski Hamamatsu R7525HA fototüplerin yerini almak üzere Hamamatsu R7600U-200-M4 modeli fototüpler seçilmiştir [1]. Yeni dört anotlu fototüpler, pencere olaylarını donanım seviyesinde belirlemeyi mümkün kılar; cama çarpan müonlar yalnız bir anotta görülür, ancak gerçek olaylar tüm anotlarda görülür. 2011 yılında, $i\phi = 67$, $i\eta = 29, 30, 31, 32$ koordinatlarına bağlı olan HF+ dedektöründeki sekiz eski fototüp yenileriyle değiştirilmiştir. Bu tezin amacı eski ve yeni fototüplerin pencereye çarpan müon olaylarına tepkisini sinyal analizi yaparak karşılaştırmaktır. Yeni fototüplerin, sadece ince pencereleri sayesinde dahi çok daha iyi gürültü performansı sergiledikleri gösterilmiştir.

TABLE OF CONTENTS

LIST OF FIGURES

LIST OF TABLES

LIST OF SYMBOLS

c	Speed of light in vacuum
E	Energy
fC	Femto Coulomb
GeV	Giga electron-volt
$\mathcal{L}$	Luminosity
MHz	Megahertz
n	Refractive index
ns	Nano second
p	Momentum
Q	Charge
T	Tesla
TeV	Tera electron-volt
ts_{max}	Peak timeslice
η	Pseudorapidity *or* Quantum Efficiency
λ	Wavelength
μm	Micro meter
π^0	Neutral pion
ϕ	Azimuthal angle

LIST OF ACRONYMS/ABBREVIATIONS

ADC	Analog to digital converter
ALICE	A Large Ion Collider Experiment
APD	Avalanche Photodiode
ATLAS	A Toroidal LHC Apparatus
CMS	Compact Muon Solenoid
CSC	Cathode Strip Chamber
ECAL	Electromagnetic Calorimeter
HB	Hadron Barrel
HCAL	Hadronic Calorimeter
HE	Hadron Endcap
HF	Hadron Forward
HO	Hadron Outer
HPD	Hybrid Photodiode
LEP	Large Electron-Positron Collider
LHC	Large Hadron Collider
LHCb	Large Hadron Collider beauty
LSP	Lightest SUSY Particle
PMT	Photomultiplier Tube
PS	Proton Synchrotron
PSB	Proton Synchrotron Booster
QIE	Charge Integrator and Encoder
RBX	Readout Box
RPC	Resistive Plate Chambers
SPS	Super Proton Synchrotron
SUSY	Super Symmetry
WIMP	Weakly Interacting Massive Particle

1. INTRODUCTION

The Large Hadron Collider (LHC), with its design center of mass energy of 14 TeV and luminosity of $10^{34} cm^{-2} s^{-1}$, is an unprecented effort to shed light on many unsolved questions of physics. The Compact Muon Solenoid (CMS), as one of the two main detectors at the LHC, enables physicists to investigate a wide range of physical theories and phonemena.

The Hadron Forward Calorimeter (HF) is an important part of the CMS, serving to improve jet detection and missing transverse energy resolution in the $3.0 < |\eta| < 5.0$ pseudorapidity region. The HF detector consists of quartz fibers embedded in steel absorbers, which generate Čerenkov light that is picked up by photomultiplier tubes (PMT).

It has been known since 2004 that muons striking PMT windows directly create high energy noise events that are difficult to identify and reject. New quad-anode PMTs were chosen to replace the old ones in the 2013 upgrade. The focus of this thesis was the comparison of the response of the old and new PMTs to window hits using pulseshape analysis. 2011 Jet data were analyzed using the ROOT framework.

The first chapter of this thesis briefly introduces the LHC. The next chapter summarizes the design, goals, and constituents of the CMS detector. The fourth chapter introduces the Hadron Forward subdetector in further detail, briefly explains the problems encountered in its operation and presents the specifics of the quad-anode PMTs. The last two chapters detail the data analysis and finish with a brief summary and discussion of the results.

2. THE LARGE HADRON COLLIDER

The Large Hadron Collider (LHC) is the largest particle accelerator in the world operating at the highest energy to date, with a current center of mass collision energy of 8 TeV as of 2012, which is expected to reach 14 TeV by around 2015, and a design luminosity of $\mathcal{L} = 10^{34} cm^{-2} s^{-1}$. The primary objective of the LHC is to investigate the Higgs mechanism which is believed to be responsible for electroweak symmetry breaking, and to study the Higgs boson through which all elementary particles are purported to obtain mass. Exploring TeV scale physics experimentally is hoped to verify the consistency of the Standard Model. Particles, forces or symmetries hitherto unknown may also manifest themselves in the high energy collisions of the LHC. Moreover, the LHC offers the possibility to glean answers to other important questions, such as those regarding CP-violation, dark matter, extra dimensions, and the Hierarchy problem.

Figure 2.1. An aerial photograph of CERN, showing the LHC and SPS rings.

2.1. Design and Construction

The LHC is a hadron accelerator and collider, capable also of accelerating heavy ions up to 2.8 TeV per nucleon with a maximum luminosity of $\mathcal{L} = 10^{27} cm^{-2} s^{-1}$, installed in a circular tunnel of 27 km circumference located at a depth between 45 m and 170 m below the ground straddling the Franco-Swiss border, which used to house the now defunct Large Electron-Positron Collider (LEP). The tunnels house two adjacent parallel rings to accelerate and contain two counter-rotating proton beams. The two rings intersect at eight points (due to the design constraints of LEP), but only at four of these do the beams actually cross, the other four beam intersections were suppressed. The LHC is not a perfect circle, with eight approximately 528-m-long straight sections, or 'insertions' connecting eight 2.45-km-long arcs. The straight sections serve as sites for beam collisions, injection, beam dumping and beam cleaning. Superconducting bending dipoles bend the beams when they pass through the arcs. There are six experiments operating at the LHC, two of which involve the high luminosity general purpose detectors; the Compact Muon Solenoid (CMS) and A Toroidal LHC Apparatus (ATLAS). The other two major experiments are the Large Hadron Collider beauty (LHCb) and A Large Ion Collider Experiment (ALICE). These four detectors reside in huge caverns built around the four beam crossings (collision sites). Two smaller detectors for TOTal Elastic and diffractive cross section Measurement (TOTEM) and the Large Hadron Collider forward (LHCf) experiments share the same caverns as CMS and ATLAS, respectively [2, 3].

2.1.1. Beam Properties

The beams produced at the LHC are not continuous, but instead consist of bursts that are 25 ns apart [4]. Each burst is called a bunch and contain approximately 1.15×10^{11} protons. Protons are initially accelerated to 50 MeV using the linear accelerator Linac 2 and fed into Proton Synchrotron Booster (PSB), which further accelerates them to 1.4 GeV and passes them onto the Proton Synchrotron (PS). Bunches are formed, and exit the PS with the correct 25 ns spacing at 26 GeV. The Super Proton Synchrotron (SPS) takes over and passes the bunches onto the LHC, at 450 GeV. The

SPS is able to fill the LHC in 12 cycles, with each beam containing up to 2808 bunches. Eight RF cavities give 0.5 MeV 'kicks' to each proton each turn. Due to the rise time of the injection and dump kickers, gaps have to be introduced into the 25 ns bunch structure, limiting the bunch crossing frequency to below the 40 MHz implied by 25 ns spacing.

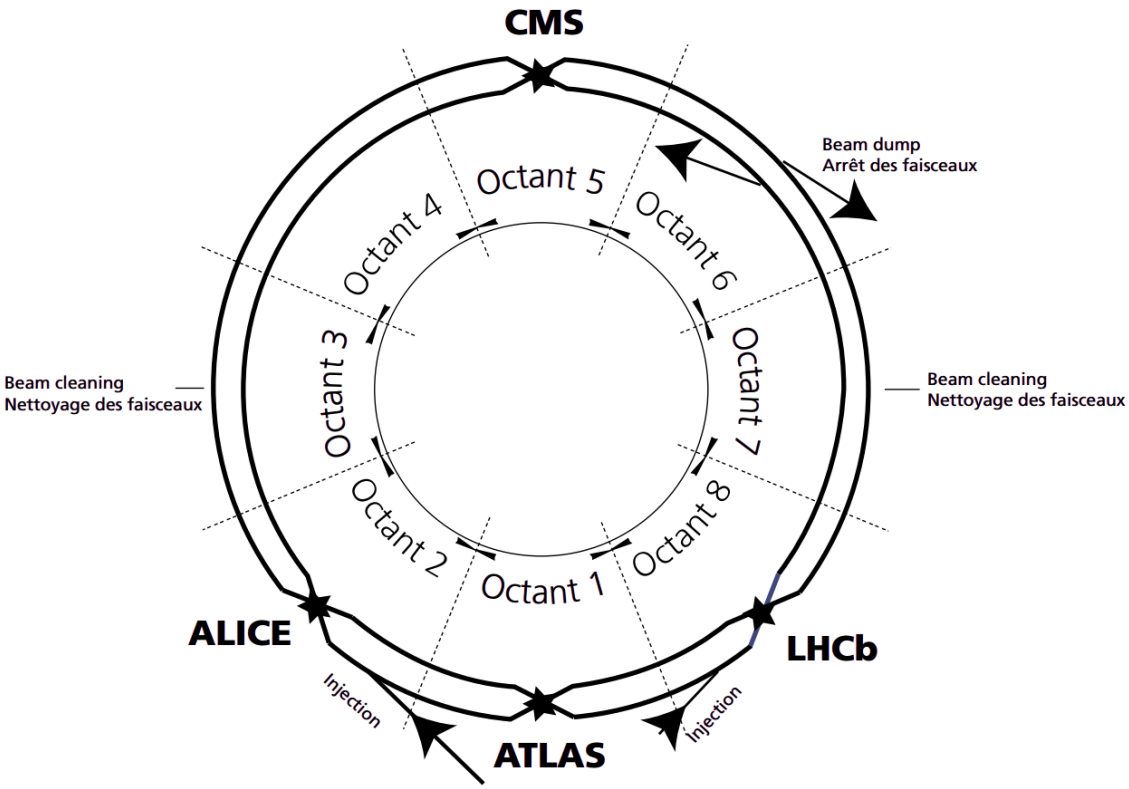

Figure 2.2. An illustration showing the octants, beam crossings, beam dump and cleaning sites, injection sites.

2.2. First Beam and Current Status

The LHC successfully circulated its first beam on 10 September 2008. Nine days later, an electrical fault led to a helium leak, resulting in over 50 magnets being damaged. More than a year later, the LHC resumed its operation and became the world's most energetic particle accelerator, surpassing the Tevatron. In April 2012, the LHC successfully reached a collision energy of 8 TeV. On the 4th of July, 2012,

CERN made an official announcement of the discovery of a new boson with a mass of 125 GeV [5], strongly suspected to be the Higgs boson. This marked an early milestone. Seven months later the LHC went into shutdown in preparation for the planned upgrade during 2013, to resume operations in 2015.

3. THE COMPACT MUON SOLENOID

The Compact Muon Solenoid is one of the two general purpose detectors installed on the LHC, designed to investigate various physical phenomena, including the electroweak symmetry breaking, supersymmetry, extra dimensions and dark matter. CMS is built around a huge 13-m-long, 5.9 m inner diameter superconducting solenoid capable of creating 4 T (nominal) magnetic fields. CMS in its entirety is a 12500 ton, 21.6-m-long detector with a diameter of 14.6 m. The powerful superconducting magnet provides CMS with the power to bend very high momentum particles such as muons, indeed the main design consideration was good momentum resolution for muons.

3.1. Physics Goals

The main goal of the CMS detector is the discovery of the Higgs boson and studying the Higgs mechanism. It is predicted that elementary particles acquire mass through interactions with the Higgs field, which will also manifest itself as a neutral spin-0 particle. The coupling of the Higgs particle is proportional to the mass of the particle it couples to, so the branching ratios of the decay modes depend on the Higgs particle mass [6], which is not predicted by the Standard Model. There are dominant decay modes in each different mass range, for which the CMS detector is finely tuned.

Another important goal of the CMS detector is the investigation of supersymmetry (SUSY). SUSY predicts the existence of supersymmetric partners to all Standard Model particles. The discovery of SUSY is important in that it will prove the validity of a unification theory. CMS looks for signs of the lightest SUSY particle (LSP). The LSP interacts weakly and is not directly observable, which is consequently why it is a dark matter candidate, and it is only detectable through missing transverse energy measurements.

By searching for weakly interaction massive particles (WIMPs) (mainly LSP), CMS also aims to investigate dark matter, which makes up about 85% of the total

mass of the total matter in the universe.

3.2. Coordinate Convention

The coordinate convention adopted by CMS has the origin at the collision point, the z-axis pointing along the beam direction, the y-axis pointing vertically upward, and the x-axis pointing radially inward toward the center of the LHC. The azimuthal angle ϕ is measured from the x-axis on the $x-y$ plane and the polar angle θ is measured from the z-axis [7]. The pseudorapidity η is defined as $\eta = -\ln\tan(\theta/2)$. The transverse energy and momenta are calculated from the x and y components. ϕ and η will be extensively used throughout this thesis, instead of the Cartesian coordinates x and y.

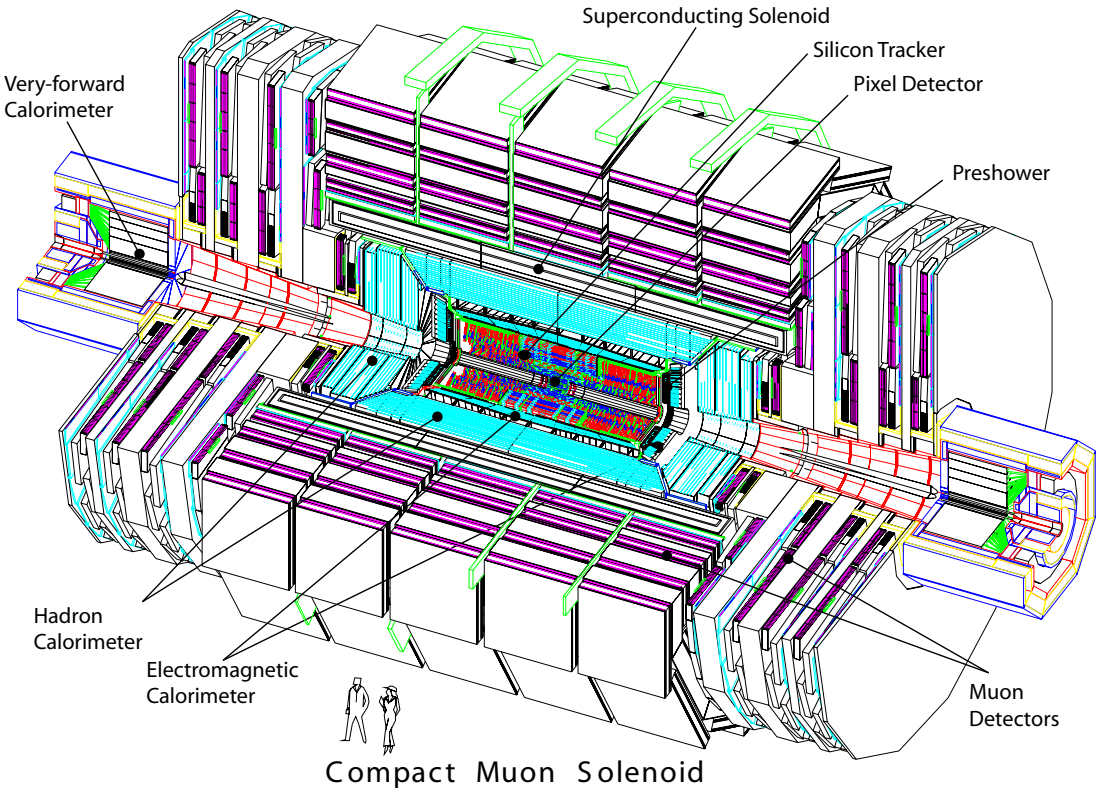

Figure 3.1. An illustration providing an overview of the CMS. It is possible to see the various detectors that make up the CMS. The Hadron Forward calorimeters are referred to as "Very-forward Calorimeters" here.

3.3. Design and Construction

CMS is comprised of multiple concentric layers. Its name alludes the fact that the tracker and calorimeters are actually inside the magnet itself, thus being compact compared to detectors of comparable weight. Apart from the Hadronic Calorimeter (HCAL) and the Electromagnetic Calorimeter (ECAL) and the silicon tracker housed inside the solenoid, there are muon chambers sandwiched between the steel return yokes.

The design of the CMS is such that the HCAL surrounds the ECAL, and the silicon tracker is inside the ECAL. The silicon tracker is the part closest to the beamline, because unlike calorimeters which fully absorb particles that try to pass through, silicon trackers interact very lightly with collision products and make it possible to construct their trajectories. The ECAL is enveloped by the HCAL, because if it were the other way around, the HCAL would absorb electrons and photons, rendering the ECAL redundant. Since electromagnetic calorimeters are not good at dealing with or containing hadronic processes, the HCAL is not significantly affected by the interference of the ECAL with hadronic products.

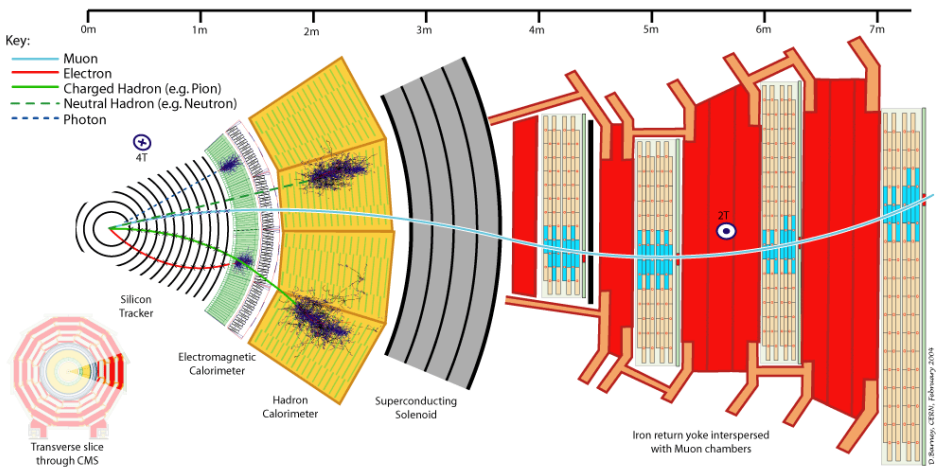

Figure 3.2. An illustration showing which particles interact with which calorimeters and how deep they are able to travel before getting absorbed. As mentioned, hadrons can be seen to largely ignore the ECAL and interact with the HCAL.

3.3.1. The Silicon Tracker

The silicon tracker is the inner-most layer of the CMS and is used to reconstruct the trajectories of charged particles after the collision allowing the CMS to reconstruct the vertices. It features 10 layers of silicon microstrip detectors, and 3 layers of silicon pixel detectors in its cylindrical body, and has two endcaps with a total of 14 layers. Each pixel is 100 x 150 μm^2 and there are 66 million of them in the 3 pixel layers. The pseudorapidity range of the silicon tracker is $|\eta| < 2.5$.

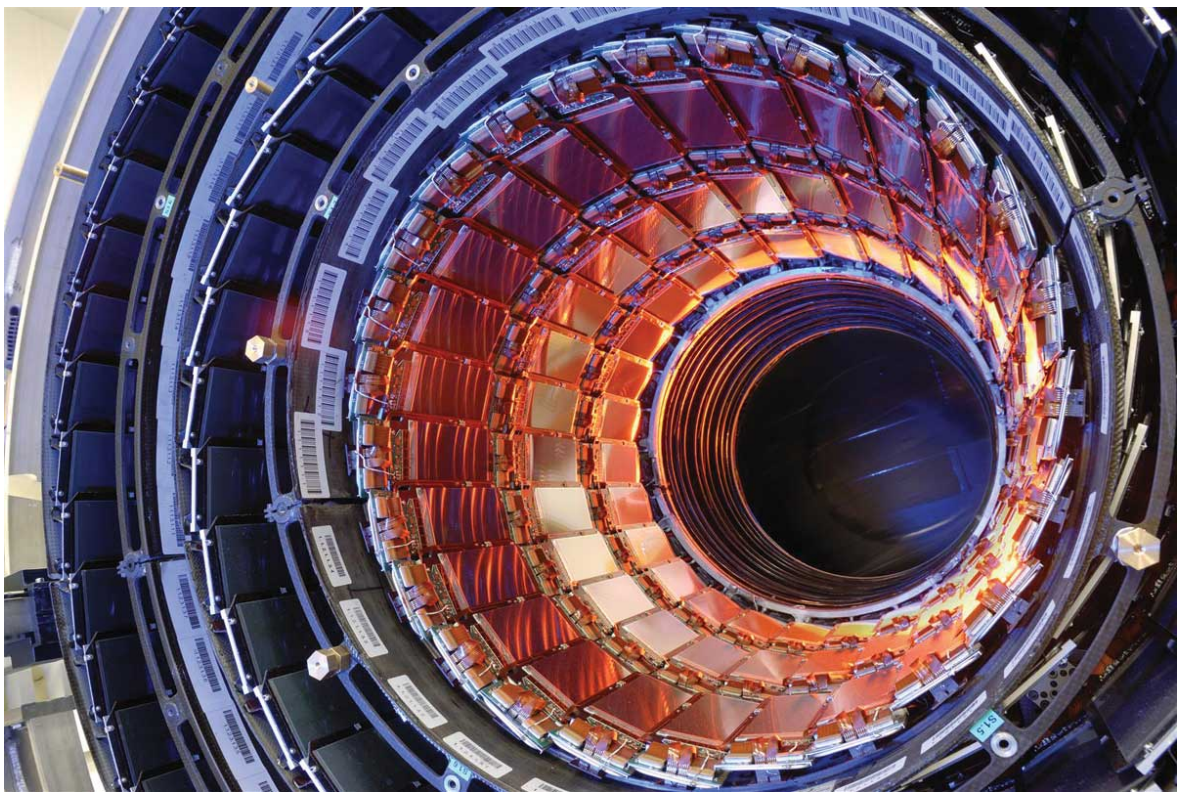

Figure 3.3. A photograph of the silicon tracker. The silicon pixel and microstrip detectors are visible.

3.3.2. The Electromagnetic Calorimeter (ECAL)

The Electromagnetic Calorimeter is a hermetic, homogenous calorimeter using lead tungstate ($PbWO_4$) crystals covering the pseudorapidity range $|\eta| < 3.0$. It is

responsible for measuring the energy of photons and electrons emerging from the collisions. It is divided into a barrel, two endcaps and an additional preshower detector. Silicon avalanche photodiodes (APDs) in the barrel, and vacuum phototriodes in the endcap section detect the scintillation light radiated from the lead tungstate crystals. A preshower detector is installed in the front of the endcap to detect and reject neutral pions. The barrel section covers the pseudorapidity region $0 < \eta < 1.48$ while the endcaps cover $1.48 < |\eta| < 3.0$.

3.3.3. The Hadronic Calorimeter (HCAL)

The Hadronic Calorimeter (HCAL) surrounds the ECAL, and is explained in detail in the next chapter.

3.3.4. The Magnet

Moving charged particles experience Lorentz force inside a magnetic field, and are deflected from their linear trajectories. Inside a magnetic field of fixed magnitude, charged particles "bend" to follow a curved path, where the radius of curvature is proportional to the momentum of the particle as dictated by the formula $\vec{F} = q(\vec{v} \times \vec{B})$. By determining the radius of curvature of the path of a particle, it is possible to calculate its momentum. The CMS solenoid magnet serves exactly this purpose, with the aid of the silicon tracker and the muon chambers.

The 4 T (nominal) solenoid magnet the CMS is built around is the biggest and most capable of its kind to date. Its inductance is 14 H, at 4 T a current of 19500 A is needed resulting in a maximum energy of 2.66 GJ.

The required bending power of the magnet is dictated by necessity to have a momentum resolution of $\Delta p/p = 10\%$ at p = 1 TeV/c to be able to correctly determine the sign for muons with momenta around 1 TeV [8].

3.3.5. The Muon System

Muon detection and measurements are essential to the operation of the CMS, since muons are among the decay products of possible new particles. One such decay mode is the one where the Higgs boson decays into four muons. Muons pass through the calorimeters without depositing much of their energy, and can even penetrate several meters of iron. As neutrinos and muons are about the only particles that can reach the outer shell of the CMS, muon detectors are placed at the outermost layer. The muon system is composed of a cylindrical barrel and two endcaps. The muon detectors are interleaved with iron return yokes. There are three different types of gaseous detectors utilized in the muon system. The barrel features drift tube systems (DT) and cover the pseudorapidity interval $|\eta| < 1.2$, where the muon rate is low. The endcaps have cathode strip chambers (CSC) which cover $0.9 < |\eta| < 2.4$. Both regions have resistive plate chambers (RPC) used for muon triggering which cover $|\eta| < 1.6$. The RPCs have both high response time and decent spatial resolution.

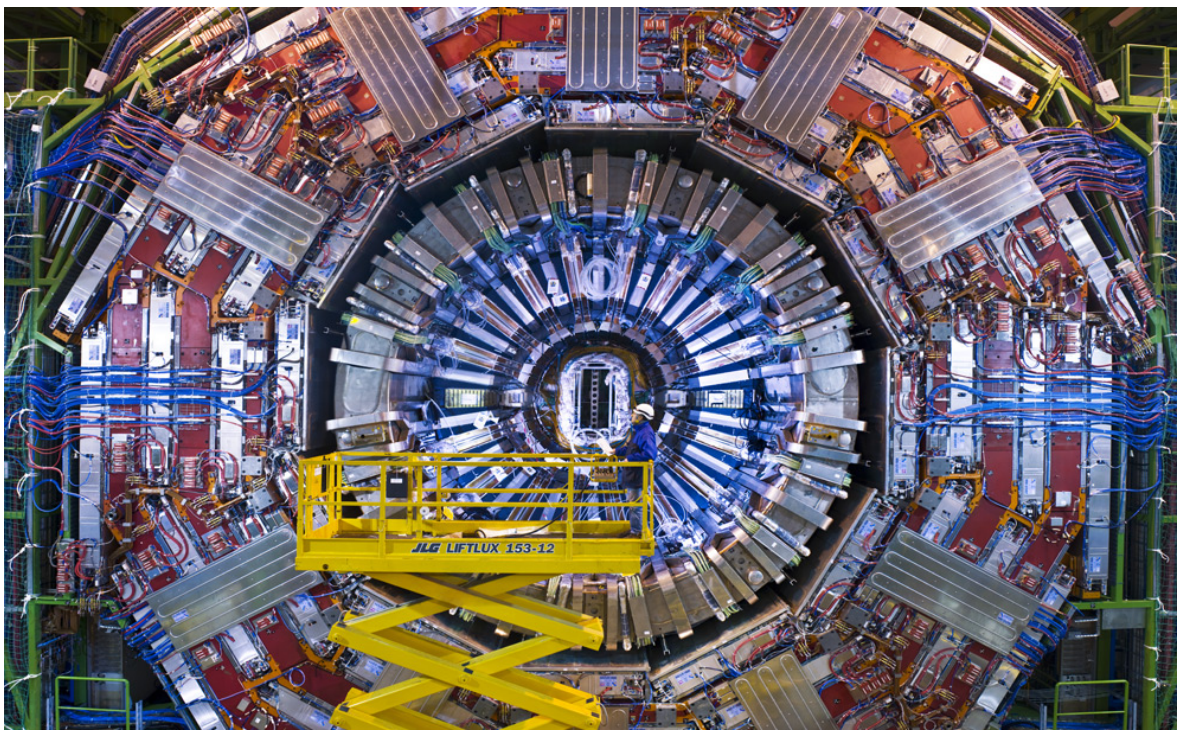

Figure 3.4. A photograph of the CMS. It is possible to make out the thick white plates which are muon detectors interspersed in the red iron return yoke.

4. HCAL CALORIMETRY

4.1. Calorimetry

Calorimetry and calorimeters, in the context of particle physics, refer to the process of identifying particles and measuring their energies, and to the apparatus designed to do so. Calorimeters fully absorb the incident particles, unlike other detectors [6, 9]. Incident particles interact with the passive media in a calorimeter, and generate secondary particles, which interact with the medium like their parent particles to create other secondary particles, forming a cascade of many particles called a "shower". For this reason, they are often referred to as "shower counters" [6]. Measuring showers makes it possible to detect neutral particles, which interact with the passive absorbers to create showers.

Calorimeters have numerous advantages over other types of detectors, especially in the high energy domain. As mentioned, they allow the detection of chargeless particles, by detecting and measuring the charged shower products. It is even possible to detect neutrinos by measuring the missing transverse energy [9]. Relative energy resolution $\Delta E/E$ is proportional to $\frac{1}{\sqrt{E}}$ in calorimeters, where E is the energy of the particle, so unlike spectrometers for which $\frac{\Delta E}{E} \sim E^2$ [6], energy resolution improves with particle energy, which makes them ideal for high-energy experiments [6, 9]. Signal production in calorimeters is very fast, which makes them useful for triggering purposes [6]. Due to the logarithmic dependence of shower length on energy, calorimeter thickness increases not linearly, but logarithmically with particle energy, making them space and cost efficient [9].

4.1.1. Types of Calorimeters

Calorimeters may be classified as homogeneous and heterogenous (sampling) calorimeters.

The main distinction between homogenous and heterogenous calorimeters is that while the passive absorber which produces the shower and the active medium which produces the signal are separate parts in a sampling calorimeter, a homogenous calorimeter consists of only one type of material which serves as both the absorber and active medium, such as a gas chamber that produces an electron shower when bombarbed with energetic electrons [9].

Homogenous calorimeters have better energy resolution, since all the energy of the incident particle is absorbed by the active medium, unlike a sampling calorimeter where a portion of the energy is lost in the absorbing (passive) medium.

Sampling calorimeters usually consist of alternating layers of passive and active media. The dense passive absorbing media produce showers when struck by particles, and the active media absorb the shower products to produce a measurable signal in the form of light or charge. Since some of the energy of the incoming particle is lost in the absorbers, only a portion of the energy is measured; the particle's energy is "sampled". The separation of active and passive parts hurts energy resolution, but provides other advantages. Absorbers and active parts can be chosen out of different materials; absorbers are usually chosen out of dense materials so that they can provide the necessary interaction lengths while keeping the detector thickness to a minimum [9], and since the active medium does not have to be of the same type, a choice suitable for the properties of the showers is possible. Sampling calorimeters are also easier to segment both longitudinally and laterally, improving spatial resolution and particle identification over homogenous calorimeters [9].

4.1.2. Electromagnetic and Hadronic Showers

High energy electrons and photons interact with matter electromagnetically via bremsstrahlung and pair production, respectively. The photons created by bremsstrahlung further produce electron positron pairs via pair production, and these products create more photons via bremsstrahlung, which go on to create yet other electron positron pairs, creating a shower consisting of many electrons, positrons and photons.

This cascade continues until the electrons and positrons fall below the treshold energy for bremsstrahlung [10]. This process is known as an electromagnetic shower.

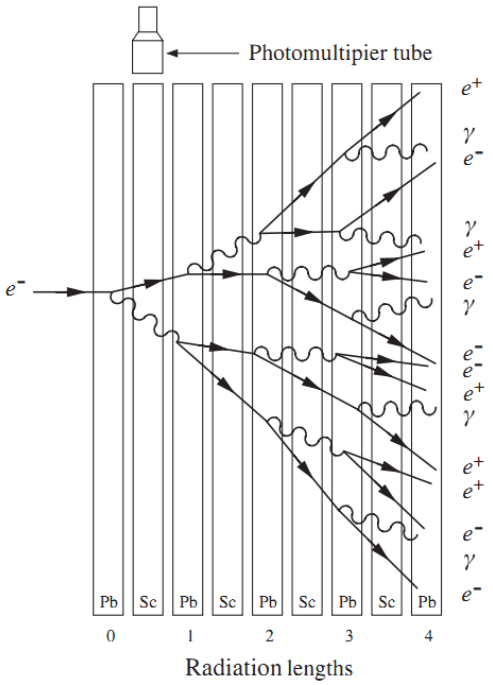

Figure 4.1. Sketch of an electromagnetic shower taking place in a sampling calorimeter with alternating layers of lead absorbers (Pb) and scintillating material (Sc) [6].

.

Hadron showers are more complex compared to electromagnetic showers. Many different processes take part in the production of secondary hadrons [6]. Secondary particles are produced mostly by strong interactions with the absorber nuclei [9]. Significant amounts of energy are lost due to nuclear excitation, nuclear breakup, evaporation, muon production, neutrino production, etc. Hence, only a small fraction of the energy of the showering hadron can usually be measured. The produced secondary particles are mostly pions and nucleons. On average, 1/3 of the produced pions are π^0's, which decay into two photons before interacting hadronically [9] and create electromagnetic showers. A hadronic shower may develop mostly as an electromagnetic shower, depending on the proportion of neutral pions produced in the early stages [6].

4.2. Detection Mechanisms

Scintillation: When charged particles hit a transparent material (or scintillating material), they excite the atoms of that material. When those atoms deexcite, they emit light, which can be measured by light detectors.

Ionization: Ionization detectors exploit the ionization of gas or liquid molecules when they are bombarded by energetic particles. The freed electrons are accelerated across a potential, which create a current that quantifies the amount of energy deposited by the passing particle.

Čerenkov Radiation: If particles travel inside a medium at speeds faster than the speed of light in the medium, they cause the medium to emit light. This is called Čerenkov radiation, and the speed of the particle depends on the azimuthal angle with respect to the direction of the incoming particle. The angle of the Čerenkov cone provides information on the speed of the incoming particles [10].

4.3. Design

The hadronic calorimeter (HCAL) is responsible for measuring hadronic jets and missing transverse energy, and combined with the ECAL forms a complete calorimetry system. It was designed to offer good hermeticity, good transverse granularity, moderate energy resolution and to be sufficiently deep so as to offer the necessary interaction length for hadron shower containment. The central barrel (HB) and endcap (HE) subdetectors completely surround the electromagnetic calorimeter (ECAL), and are in turn surrounded by the magnet, which is why they contain non-magnetic materials. The hadron outer calorimeter (HO) improves missing transverse energy measurement, and is located outside the magnet. The hadron forward (HF) detector which lies 6 m downstream of the HE endcaps extends the hermeticity of HCAL to a pseudorapidity of 5, further improving missing transverse energy measurement. It is interesting to note that to ensure good hermeticity, cable and service paths are kept to a minimum, making the detectors truly compact, but harder to design and maintain. Any leaks or

absorption by unwanted materials hampers the performance of the detector.

The following subsections summarize the constituents of the HCAL, while the HF detector is introduced in detail in the following chapter.

4.3.1. Hadron Barrel

The hadron barrel calorimeter (HB) is a sampling calorimeter consisting of two half barrels, divided into 18 $\Delta\phi = 20°$ "wedges". Each wedge contains 5 cm thick brass alloy absorber plates oriented parallel to the beam axis, with the exception of the innermost and outermost absorber plates which are made of stainless steel. Between the absorber plates are active scintillator tiles made of plastic. The tiles are connected to wave-length shifting fibers (WLS), which are connected to clear fibers, which relay the optical signal to pixelated hybrid photodiodes (HPD). The HB is responsible for the pseudo-rapidity range $|\eta| < 1.4$.

4.3.2. Hadron Outer

The barrel calorimeter, due to various constraints, is less than a meter deep, which does not provide a sufficient interaction depth. To make up for this shortcoming, the first muon absorber layer is fitted with scintillator tiles like those found in the barrel section, to form the hadron outer (HO) calorimeter. The geometry of the scintillators is identical to those found in the HB, and have separate optical readout. The HO calorimeter has two coarse sampling layers and hermetically compliments the barrel calorimeter to achieve full hadron shower energy containment, specifically accounting for late shower development. It covers the pseudorapidity region $|\eta| < 1.3$.

4.3.3. Hadron Endcap

The endcap calorimeter (HE) covers the pseudo-rapidity range $1.3 < |\eta| < 3.0$. It is composed of brass absorbers and plastic scintillators just like the HB and the HO. While the thickness of the brass plates and plastic scintillators differ from those of the

HB's, the geometry and tiling is almost identical. The HE consists of two parts, both of which interlock with the HB on either side along the beam axis.

5. HADRON FORWARD CALORIMETER

The Hadron Forward (HF) calorimeter consists of two identical calorimeters placed on either side of the HCAL, and are responsible for covering a wide pseudorapidity range of $3.0 < |\eta| < 5.0$. The HF calorimeters employ quartz fibers and photomultiplier tubes instead of hybrid photodiodes like the rest of the HCAL, due to the extremely high radiation doses (up to 100 Mrad/yr) and neutron fluxes (up to 10^{16} neutron/ (cm^2 yr)) they are subjected to at high pseudorapidities [11]. The HF calorimeters vastly improve jet detection and missing transverse energy resolution which are crucial for Higgs, top quark and SUSY studies.

5.1. Design and Structure

The HF calorimeter consists of 5 mm thick steel absorber plates with a matrix of grooves separated by 5.0 ± 0.1 mm center-to-center which accommodate quartz fibers, the active part of the HF, that run parallel to the beamline. The fibers consist of a fused-silica core with a polymer hard-clad coating. The core diameter is 600 ± 10 μm, and together with a protective acrylate buffer the fiber diameter becomes 800 ± 30 μm [12].

Only half of the fibers run over the full depth of the absorber, which is 165 cm or 10 interaction lengths, and as such are called "long" fibers. The other half start 22 cm after the front of the detector, and are called "short" fibers. These long and short fibers alternate in the groove matrix, and help to distinguish between electromagnetic and hadronic showers, since products of electromagnetic showers deposit most of their energy in the first 22 cm of the detector. Each fiber bundle is connected to its own PMT, so long and short fibers are read out separately.

Each HF calorimeter, namely HF+ and HF-, is a cylindrical steel structure located 11.15 m from the interaction point with an outer radius of 130.0 cm. The steel absorber plates and fibers are bundled into modular wedges, each spanning 20° az-

imuthally. Naturally, to cover 360°, there are 18 wedges each, in HF+ and HF-. In each wedge, the fibers are bundled to form 0.175 × 0.175 ($\Delta\eta \times \Delta\phi$) towers. Each tower covers 10°, except for the two towers closest to the beamline, which extend over 20° (Table 5.1).

Figure 5.1. Modular HF wedges.

The virtual coordinates $i\eta$ and $i\phi$ are used to refer to each tower. $i\eta$ values range from 29 to 41, with 41 being the closest to the beam. $i\phi$ takes only odd values and range from 1 to 71. It is important to note that channels with $i\eta = 40$, 41 are only present at $i\phi = 3 + 4$n with n = 0, 1, 2, . . . , since each wedge has only one $i\eta = 40$ or 41 tower (Figure 5.2).

The fibers connect to air-core light guides, which penetrate through almost a meter of shielding consisting of steel, lead and polyethylene to reach the PMTs, housed in readout boxes (RBX). The light guides, essentially hollow tubes inlined with custom made reflective sheets, are designed to be efficient, yet almost half the light is lost before reaching the PMTs. Every wedge has two RBXs servicing it, housing 24 PMTs each. This makes for a total of 1728 PMTs or channels, in HF+ and HF- combined.

Table 5.1. Sizes, η and ϕ ranges, virtual coordinates for HF towers.

iη	η range		Size	
	η_{low}	η_{high}	$\Delta\eta$	$\Delta\phi$ $(Degrees)$
29	2.853	2.964	0.111	10
30	2.964	3.139	0.175	10
31	3.139	3.314	0.175	10
32	3.314	3.489	0.175	10
33	3.489	3.664	0.175	10
34	3.664	3.839	0.175	10
35	3.839	4.013	0.174	10
36	4.013	4.191	0.178	10
37	4.191	4.363	0.172	10
38	4.363	4.538	0.175	10
39	4.538	4.716	0.178	10
40	4.716	4.889	0.173	20
41	4.889	5.191	0.302	20

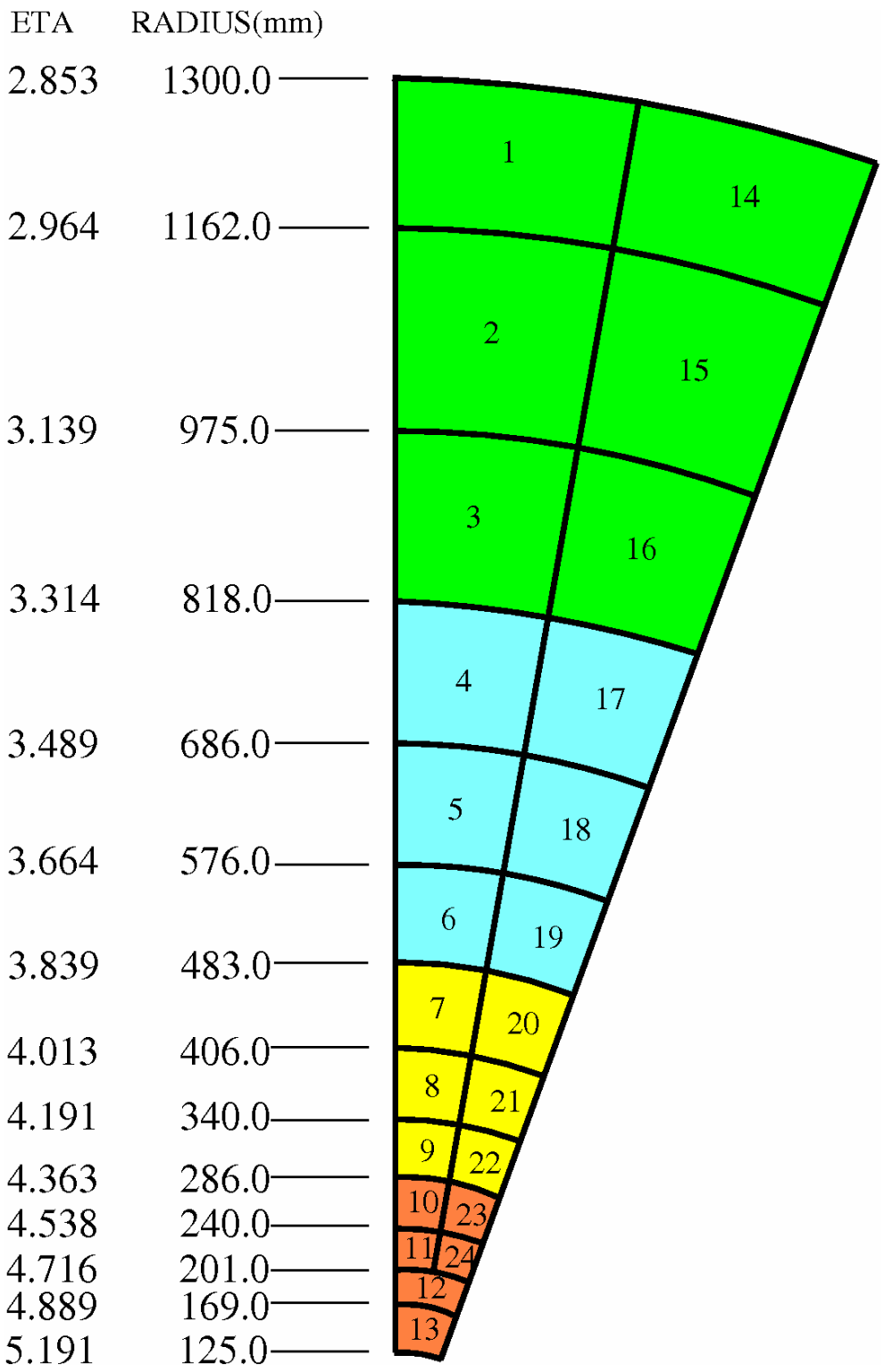

Figure 5.2. Illustration showing the HF tower structure.

The readout boxes house PMTs which are connected to electronic backboards. Analog to digital converters called QIEs (Charge integrator and Encoder) digitize the signals, producing what is referred to as "ADC count". A conversion factor for each PMT is known, and is used to convert ADC counts to charge values (fC) and the calibration constant for each PMT is used to calculate the total energy in a hit.

5.2. Čerenkov Calorimetry

Relativistic charged particles produced by hadron or electron showers radiate Čerenkov light when they pass through quartz fibers, and some of this light travel along these fibers to photomultiplier tubes. The main advantage of a Čerenkov quartz calorimeter over a scintillation or ionization based one is its high radiation resistance [11]. Quartz fibers, coated with radiation resistant cladding, make it possible for the HF calorimeters to withstand the massive amounts of radiation delivered at the high psuedorapidities they operate, where years of reliable operation is crucial to the performance of the CMS. The HF calorimeters receive 760 GeV per pp collision, compared to 100 GeV for the rest of the CMS [12, 13]. It is expected that an accumulated radiation dose of 1 GRad over 10 years will result in loss of optical transmission by half [12].

Čerenkov calorimeters also have sensitive regions much narrower compared to scintillation calorimeters [11]. This feature is very important for reconstructing narrow hadronic jets. They also produce short, sharp signals, so much so that the signal width is dependent on the response characteristics of the photodetectors employed. Apart from being radiation resistant, Čerenkov calorimeters are a lot less sensitive to neutrons (only charged particles can create Čerenkov radiation) and decay products, helping to improve background suppression.

5.3. Photomultiplier Tubes

Photomultipliers are extremely sensitive light detectors. PMTs are usually evacuated tubes which contain a series of dynodes between a photosensitive cathode and

an anode. Photons incident on the photocathode are converted to electrons via the photoelectric effect, and these electrons are accelerated through a series of terminals held at high voltages called dynodes to create secondary electrons, which strike other terminals farther down the tube to create an electron cascade, amplifying the signal created by the original photons, typically by a factor on the order of 10^6 [10]. PMTs create fast, sharp signals, have low noise, and are so sensitive tha they can detect even single photons.

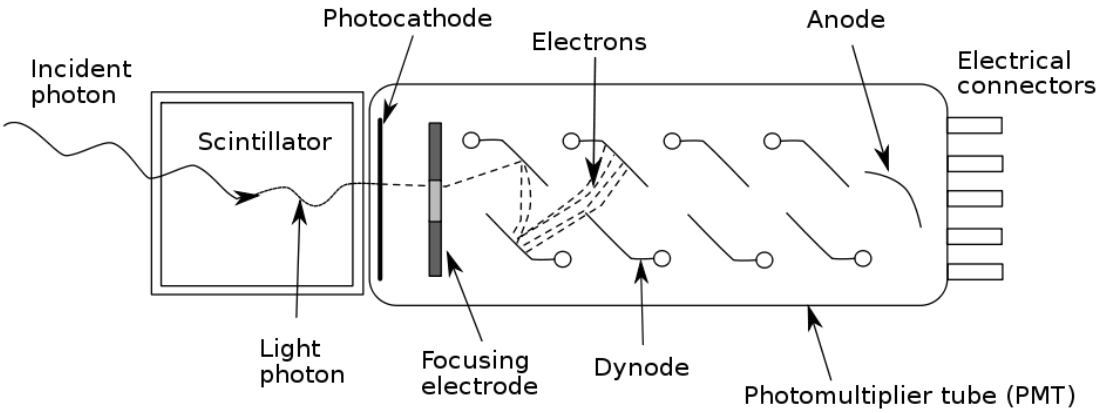

Figure 5.3. The structure and operation of a PMT [14].

A relevant property mentioned in this thesis is the quantum efficiency of a PMT. Quantum efficiency is the efficiency of photoelectric conversion of incident photons to photoelectrons, which varies with the type of material the cathode is made out of, and the incident photon wavelength. The quantum efficiency $\eta(\lambda)$ is [10],

$$\eta(\lambda) = \frac{\text{number of photoelectrons released}}{\text{number of incident photons}(\lambda)}$$

where λ is the wavelength of light. Since the quantum efficiency of a PMT depends on the wavelength, the maximum quantum efficiency is often cited in technical specifications.

5.4. Processing PMT signals

The PMTs in the HF calorimeter are connected to electronic baseboards, which have a certain type of analog to digital converters (ADC) called QIEs (Charge Integrater and Encoder). QIEs have four capacitors that collect charge in succession from the PMT during 25ns intervals. The charges are summed and encoded to a seven bit digital signal, this is referred to as the ADC count [12]. It is important to note that the ADC count does not increase linearly with measured charge, but instead it varies logarithmically. A conversion table which lists the amount of charge in units of fC corresponding to an ADC count value is employed to convert back to charge.

The pulseshape of a PMT signal is divided into 25ns intervals referred to as "timeslices". The amount of timeslices during which data are recorded may vary from run to run. Since the response of the HF is very fast and sharp, most of the energy of a pulse is contained within a few timeslices, with one timeslice exhibiting a very sharp and prominent peak for a healthy pulseshape. Through phase calibrations, the exact timeslice in which the signal should arrive is known, and should be the same for all PMT hits in the same run.

5.5. Problems in the HF Calorimeter

5.5.1. PMT Afterpulse

Afterpulses are unwanted pulses that appear after a true signal. The main cause of an afterpulse is the ionization of leftover gases, or ambient gases which have seeped into the PMT. Ionization afterpulses arrive after a delay, usually of the order of a few hundred nanoseconds [15].

5.5.2. Muon Hits on the PMT Window

Ideally, the PMTs in HF should be receiving Čerenkov light from the quartz fibers. In some cases, however, relativistic charged particles may hit a PMT window

directly, despite their location behind shielding. These charged particles, mostly muons, induce Čerenkov radiation as they traverse the PMT window and create a high energy signal, and thus are sometimes referred to as window events. Despite their low rate, these events may skew missing transverse energy measurements. Energy deposition by window hits is on the order of a 100 GeV, so the effect is significant [16]. They also mimic high-energy events, and affect triggering decisions, resulting in a lot of junk data to be committed to disk, and increase the dead time, causing proper events to be missed.

5.5.3. Handles on Window Hits

Muon hits are characteristically early and have localized energy deposition. These facts may be used to distinguish between real hits and window hits.

The Čerenkov mechanism provides a very fast response time. The Čerenkov photons travel inside the fibers at the speed of light in vacuum divided by the index of refraction of quartz. Muons causing window hits bypass the fibers and hit the PMT window directly, so they arrive about 5 ns earlier than normal hits [16].

Showering particles, due to the proximity of the long and short fibers, create signals in PMTs attached to both fibers simultaneously. The energy deposition in the long and short fibers from late showering particles should be about the same. Evaluating the ratio $\frac{S}{L+S}$ where S is the energy reading in the short fiber channel and L is the energy value for the long fiber channel, can help identify if there is an energy discrepancy between L and S. It is important to note, however, that this ratio might be low due to early showering particles, such as electrons. Simply using this ratio to impose a cut causes proper hits to be rejected. Another study suggests comparing pulse widths to identify muon hits [17]. Čerenkov signals typically produce asymmetric pulseshapes with at least 4 ns width. Muon hits, however, produce symmetric pulses that are narrower ($\sim$2 ns). This, combined with the other rejection/tagging methods may help mitigate the problem created by window hits.

Table 5.2. Single and 4-anode PMT specifications.

PMT Model	R7525HA	R7600U-200-M4
Photocathode	Bialkali	Ultra Bialkali
Quantum Efficiency (max. %)	25	43
Typical Gain	5.0×10^5	1.3×10^6
Window Area	490 (round)	324 (square)
Window Thickness	1 mm (center) 6.1 mm (at the edges)	< 1 mm

5.6. 4-Anode PMTs

To cope with the noise created by window hits, the new quad-anode PMTs were selected to replace the current ones in the HF during the 2013 upgrade. They are significantly different compared to their predecessors. The new PMTs feature a window segmented into four quadrants. Each quadrant has its own set of dynodes and output channels. In addition to being segmented, the window is significantly thinner (< 1 mm) and smaller compared to that of the old PMTs (Table 5.2).

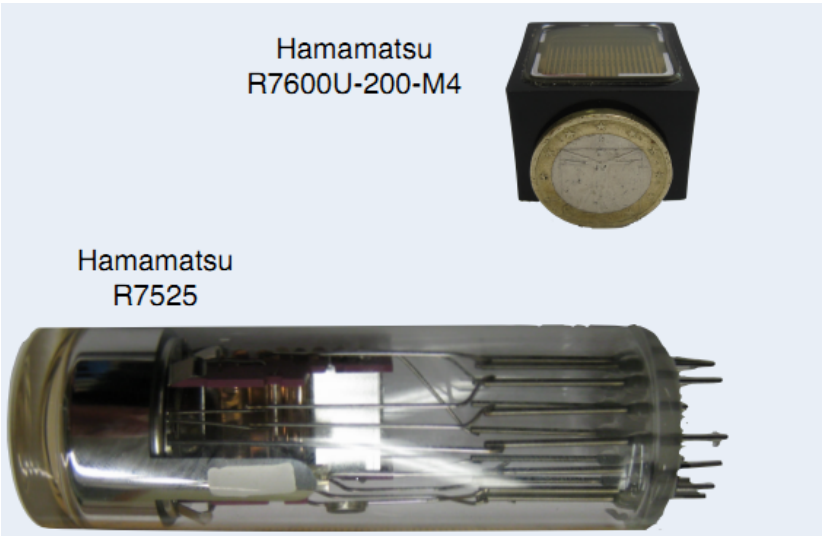

Figure 5.4. The single and quad anode PMTs.

5.6.1. Response to Window Hits

On account of their thinner and narrower windows, the new quad-anode PMTs are expected to reduce the number of window events, since a thinner window means less interaction and a reduced energy deposition, and a smaller surface area reduces the probability of a window hit for obvious reasons. In addition to these advantages, having 4 channels inside one PMT also makes it possible to investigate the localization of energy deposition in one single PMT. If only one quadrant is illuminated, this immediately points to a window hit, since Čerenkov light coming from the fibers would illuminate all four quadrants. There are however practical and financial constraints on the amount of readout channels HF can accommodate, so all four quadrants may not be separately readout in the final setup. Regardless of this, the properties of the window are expected to help significantly with the window hit problem.

In 2011, a single RBX that houses eight of these new PMTs was installed in the HF+ for testing purposes. The PMTs are servicing the wedge $i\phi = 67$, towers $i\eta =$ 29,30,31,32. This location was selected in order to minimize the impact on physics analysis since very few hits are recorded at these η values. All these new PMTs, except for the one at $i\eta = 29$ have their outputs merged into one readout channel, meaning they are all readout like single anode PMTs. The $i\eta$=29 PMT has its outputs merged into a pair, each anode pair being readout as a long, or short channel (meaning $i\phi$=67 $i\eta = 29$ Depth=1,2 are actually the outputs of a single PMT, which is connected to long fibers). These channels are hidden in the data by default so as to exclude them from physics analysis, although a configuration file may be employed to "activate" these channels.

The purpose of this thesis was to compare the new 4-anode PMTs to the old ones by employing pulse shape analysis. Due to the way they are readout, the channels $i\phi$=67 $i\eta$=29 Depth=1,2 were excluded from the analysis. 2011 Jet data were used to analyze the response of PMTs to real events.

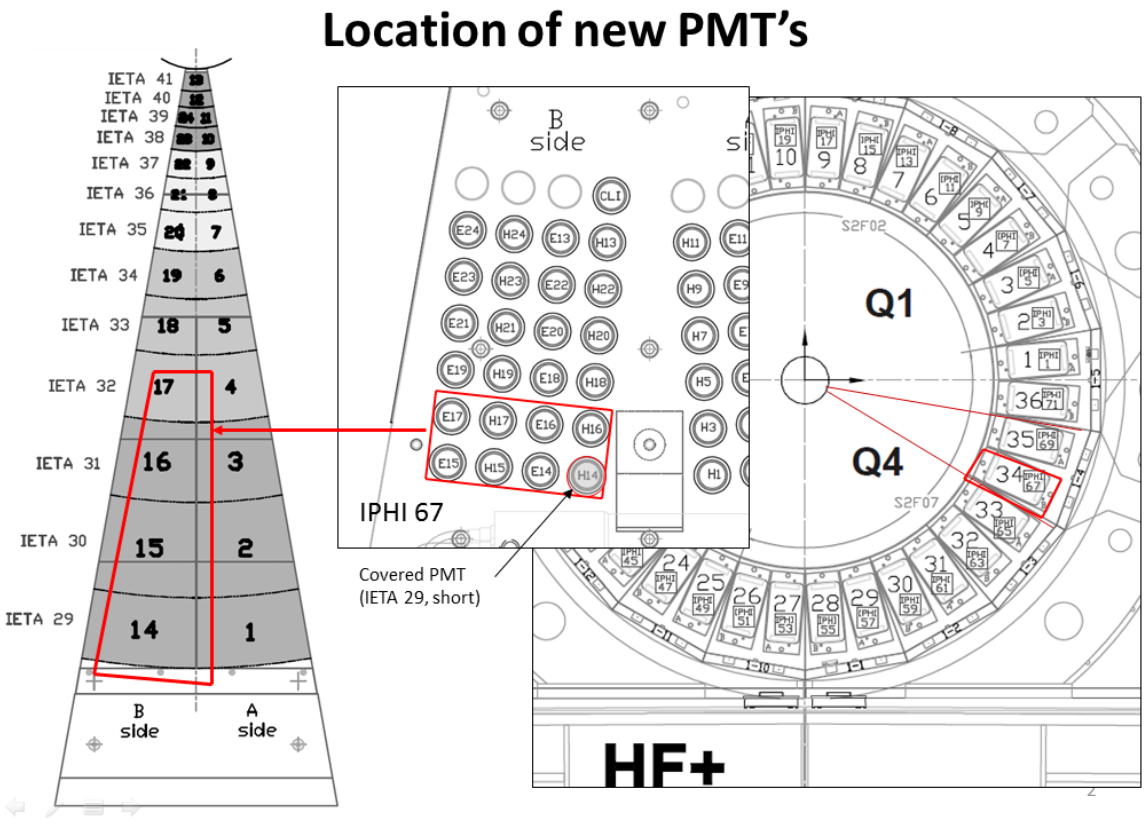

Figure 5.5. Schematics showing the location of the eight PMTs installed in the HF+.

6. DATA ANALYSIS

To distinguish noise hits from proper hits, pulse shape analysis was employed. The pulse shape of a proper hit has a narrow sharp peak in the exact timeslice set for that run. The number of timeslices used, and the timeslice number with the highest charge measurement corresponding to the respective run are presented below in Figures 6.1-6.3. It is important to note at this point that a minimum energy threshold of 20 GeV was imposed on all histograms.

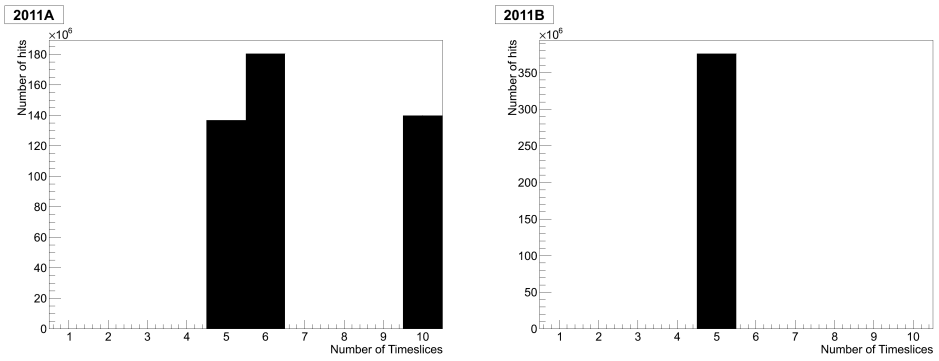

Figure 6.1. Histograms showing the number of timeslices present in runs in the 2011A,B Jet data.

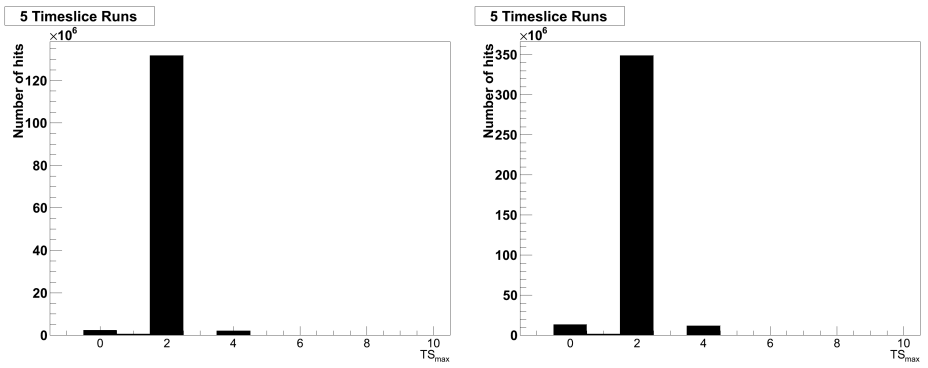

Figure 6.2. Histograms showing distribution of timeslice corresponding to maximum charge (ts_{max}), in 5 timeslice runs for the 2011A (left) and 2011B (right) datasets.

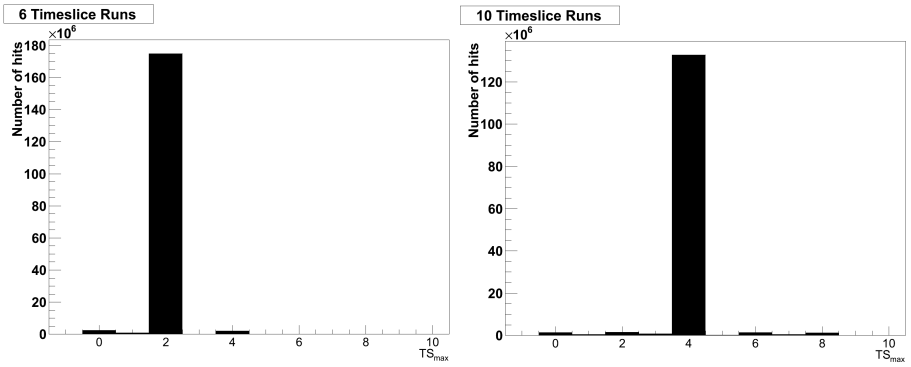

Figure 6.3. Histograms showing distribution of timeslice corresponding to maximum charge (ts_{max}), in 6 (left) and 10 (right) timeslice runs in the 2011A dataset.

A misshapen pulse has a peak outside the proper timeslice or a spread around the main peak. The ratio of the measured charge of the main peak to the sum of the charges of the three timeslices around the peak (including the peak) was chosen as a parameter to gauge the health of each hit. This ratio is defined as:

$$R = \frac{Q_{ts_{max}}}{Q_{ts_{max-1}} + Q_{ts_{max}} + Q_{ts_{max+1}}}$$

Examples of proper and noise hits are presented below (Figure 6.4).

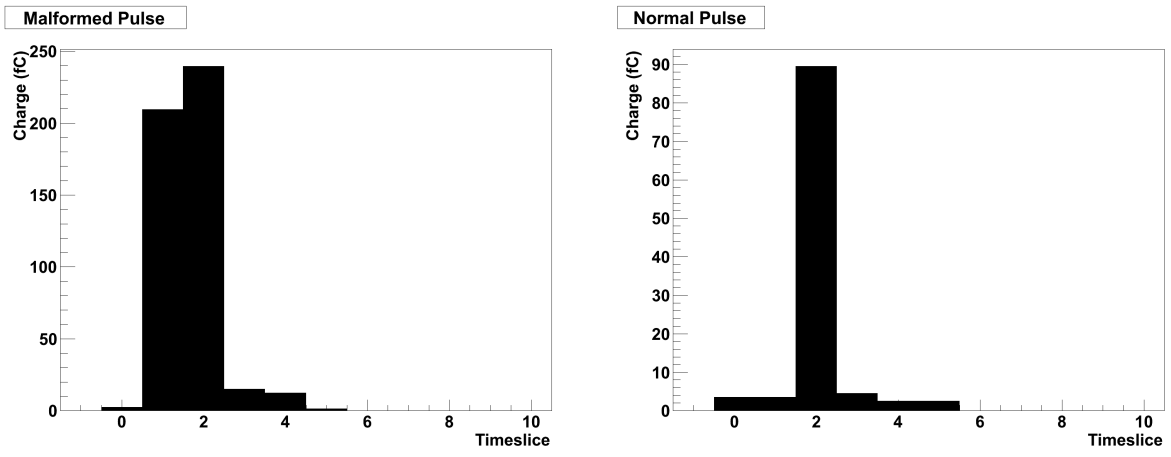

Figure 6.4. Normal and malformed pulses side by side.

To determine the distribution of noise hits, the spectrum of the ratio mentioned above, hereafter referred to as R, was plotted (Figure 6.5). As expected, a tall peak at approximately 0.9, very close to 1, is observed with a tail nearly reaching 0.6. A conservative value of 0.7 was chosen as the threshold for noise/hit identification, with hits having an R value below 0.7 being flagged as noise.

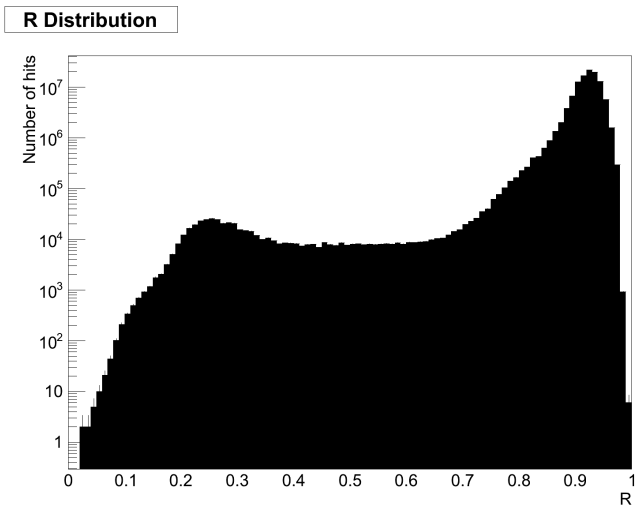

Figure 6.5. Distribution of the ratio R.

As mentioned, due to azimuthal symmetry, the hit rate is not dependent on ϕ (Figure 6.6). It does, however, depend on the polar angle η (Figure 6.7). A three dimensional plot is also presented in Figure 6.8. It was deemed appropriate to remove the η dependence from channels with the same $i\phi$ value, so that when examining the η distribution of noise for $\frac{i\phi=67}{<i\phi>}$ ($< i\phi >$ does not include $i\phi = 67$), any discrepancy between the hit/noise rates of two channels could safely be attributed to the type or characteristics of the associated PMTs. To remove the η dependence from an η distribution for a certain $i\phi$ value, said distribution was divided by the ϕ average of all hits (excluding the $i\phi$ of interest and $i\phi$=67). Noise and signal distributions were observed to have their own η dependence. The η dependence of signal and noise distributions (Figure 6.9), as well as their η-independent forms (Figure 6.10) can be seen in the histograms given below. When calculating the $i\phi$ average of a distribution, $i\phi = 67$ was never included, on account of the new PMTs at $i\eta = 30, 31, 32$.

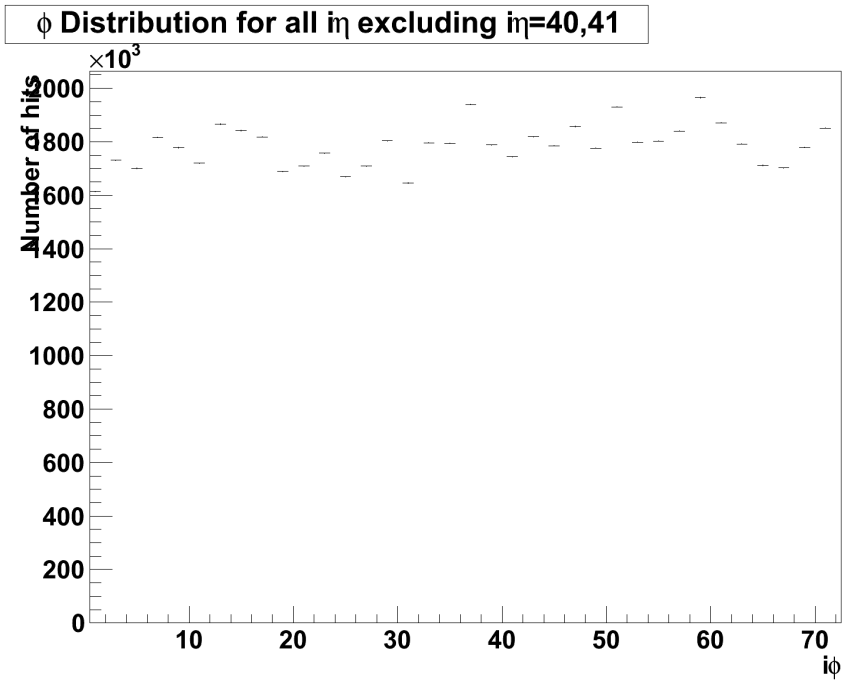

Figure 6.6. ϕ distribution of hits for all $i\eta$, HF+ , Depth = 1. Since $i\eta = 40, 41$ are at only 18 $i\phi$ values out of 36, these were excluded.

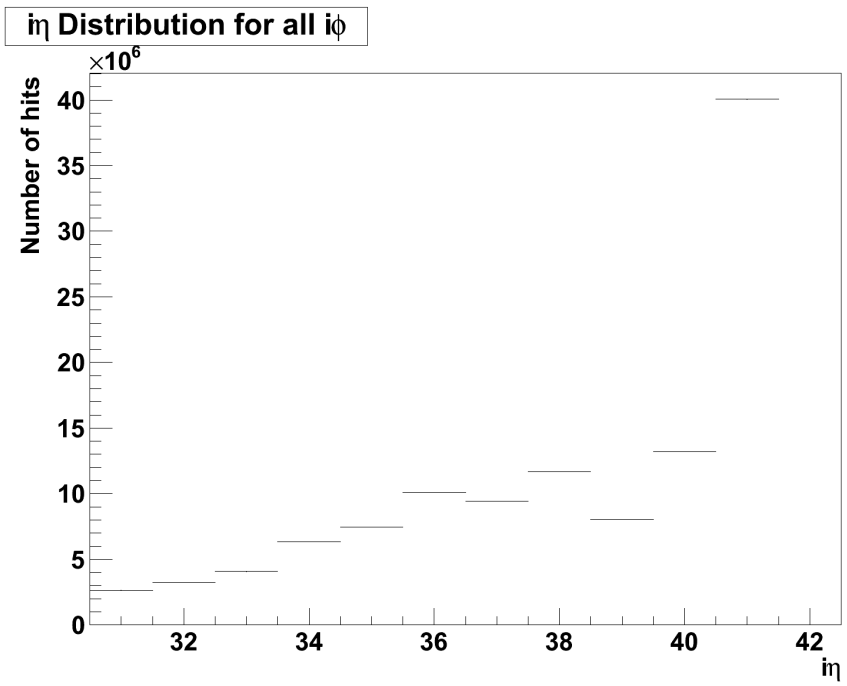

Figure 6.7. η distribution of hits for all $i\phi$, HF+ , Depth = 1.

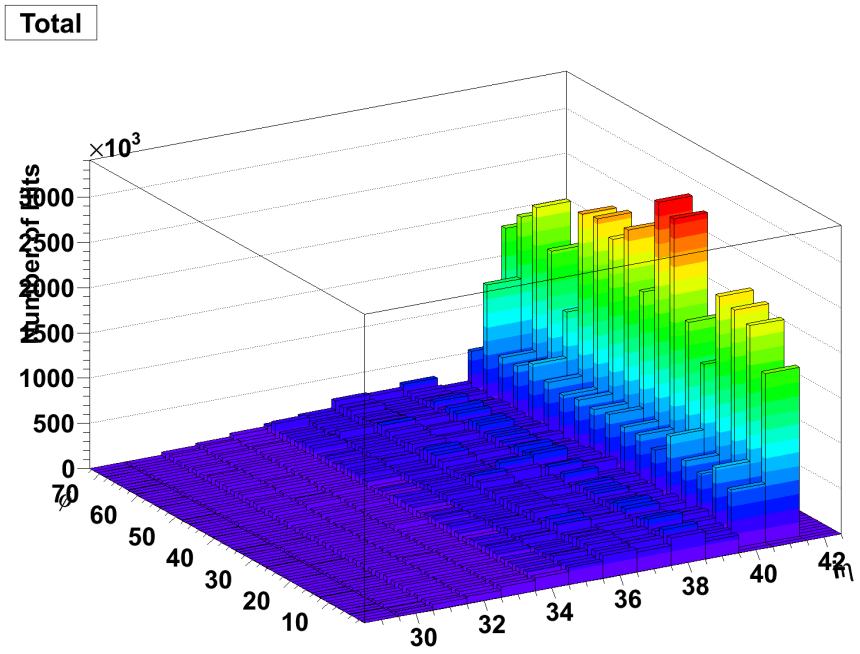

Figure 6.8. Two dimensional histogram showing the η and ϕ distribution of hits, HF+, Depth = 1.

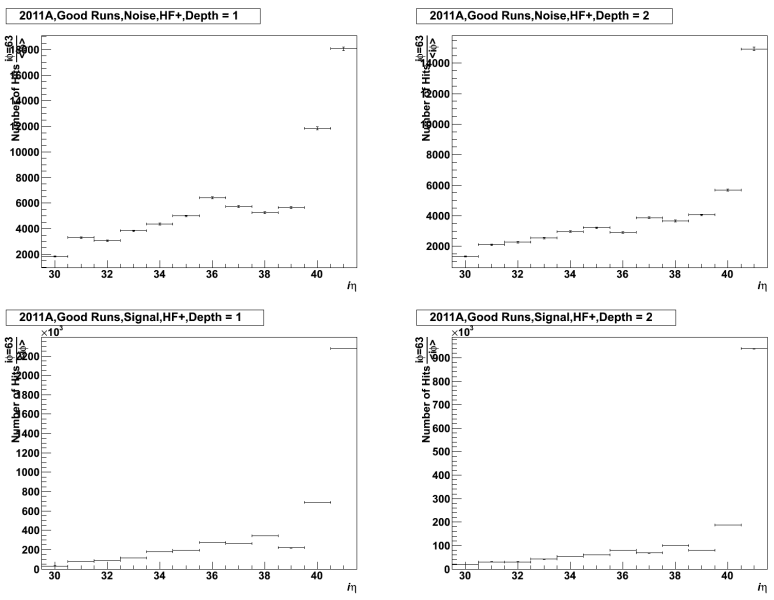

Figure 6.9. η distribution of hits for $i\phi = 63$. The top histograms are for noise hits, the histograms on the bottom are for signal hits.

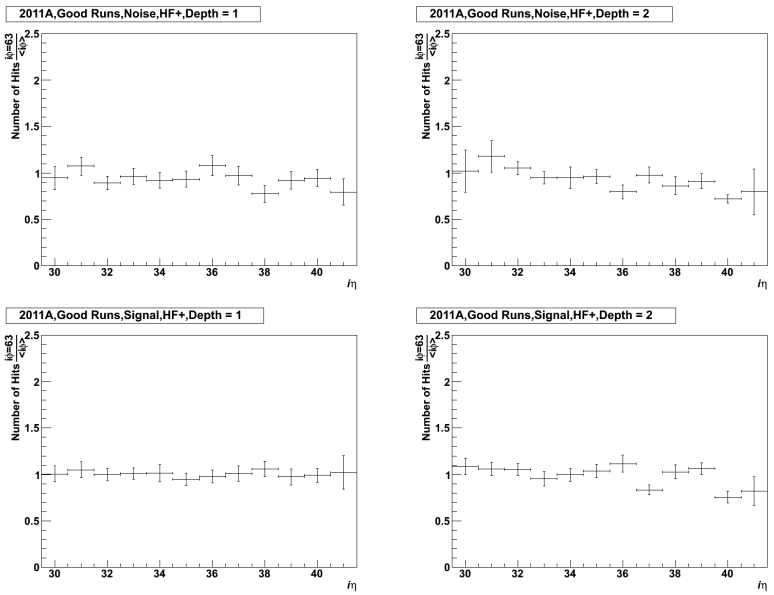

Figure 6.10. η distribution of hits for $i\phi = 63$, divided by that of $< i\phi >$. This removes the η dependence. The top histograms are for noise hits, the histograms on the bottom are for signal hits.

Checking the flattened η distribution of $\frac{i\phi=67}{<i\phi>}$ at HF+ reveals that the average noise rates for the $i\eta$ channels accommodating the new PMTs (namely 30,31,32) for the 2011B dataset are significantly lower (by a factor of 2) compared to the other channels which are single anode PMT channels (Figure 6.11). The same histogram for the 2011A dataset, however (Figure 6.12), does not exhibit a similar result; the distribution is completely flat, the noise rate for new PMTs at $i\eta = 30, 31, 32$ seem to be close to one. The same histograms for signal hits are also presented for comparison.

At this point, this discrepancy was attributed to bad runs, and η distributions for the 2011A dataset were analyzed run by run to weed out faulty runs. η distributions for all ϕ values for each run were generated, and only those that displayed the normal eta dependence were flagged as good runs. Sample good and bad η distributions pertaining to particular runs are given below, see Figures 6.13 and 6.14.

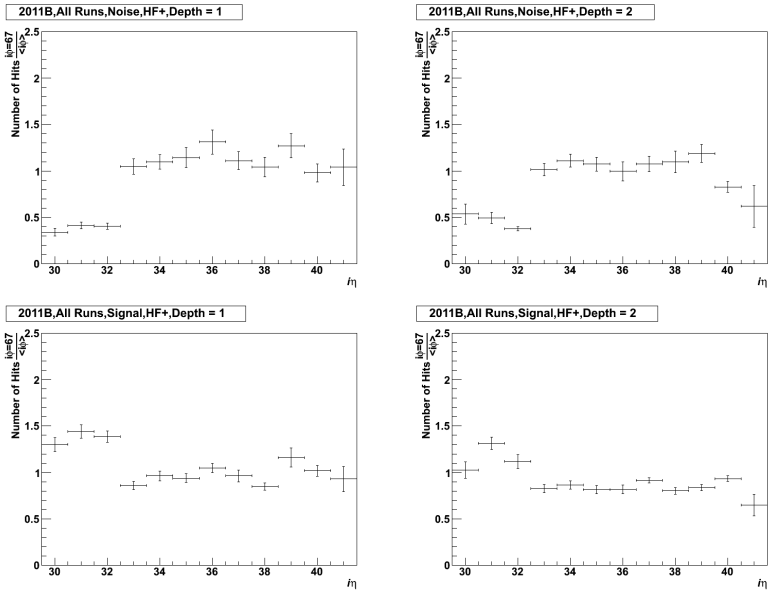

Figure 6.11. Average noise and signal rates for HF+ $i\phi = 67$ for the 2011B dataset. The top histograms are for noise hits, the histograms on the bottom are for signal hits.

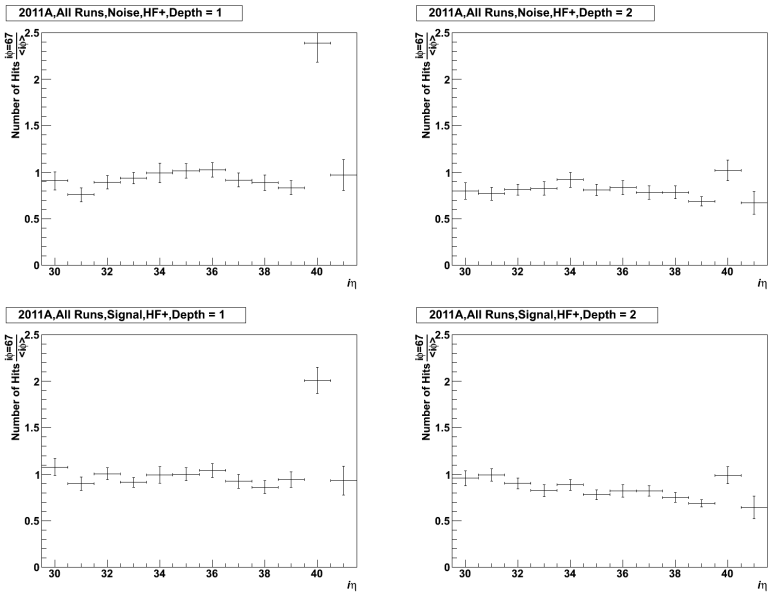

Figure 6.12. Average noise and signal rates for HF+ $i\phi = 67$ for the 2011A dataset. The top histograms are for noise hits, the histograms on the bottom are for signal hits.

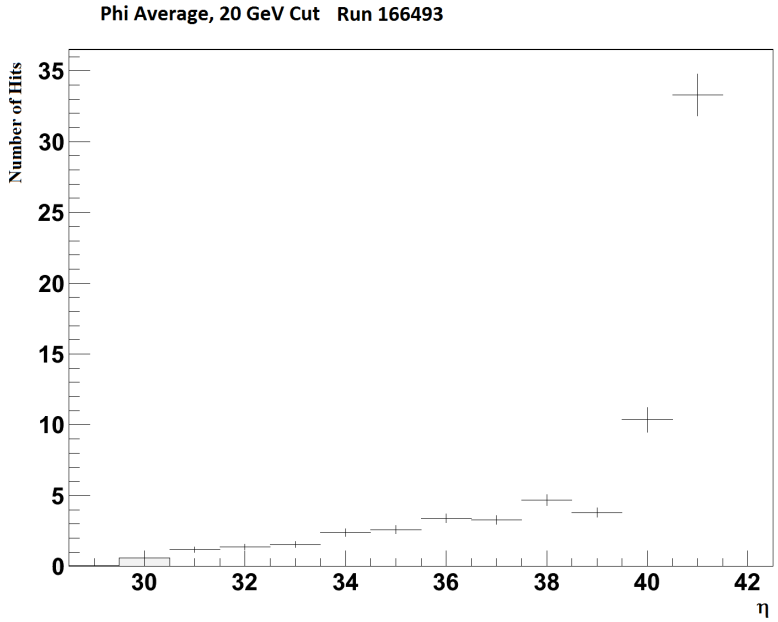

Figure 6.13. An example for a good (normal η distribution) run. Number of hits vs η distribution averaged over all ϕ from run 166493 in the 2011A jet data.

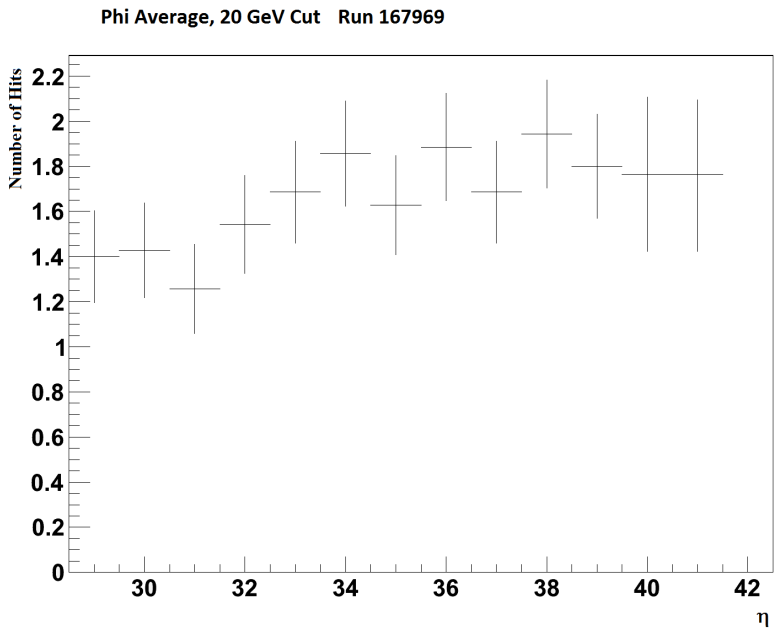

Figure 6.14. An example for a bad run. Number of hits vs η distribution averaged over all ϕ from run 167969 in the 2011B jet data. This run was rejected.

Out of 522 runs in the 2011A Jet dataset, 259 were flagged as bad runs and were excluded from the analysis. The same run by run analysis was conducted for the 2011B dataset to flag 62 runs as bad out of a total of 242. These exclusions rendered the result for the 2011A dataset very similar to the 2011B one, as expected. The 2011B result did not change by that much, which is to be expected since the ratio of bad runs to good runs is not that high compared to the 2011A dataset. It is important to note that these bad runs were present, even after using the lists of good runs. The results for the 2011A and 2011B datasets, after elimination of bad runs are given below. The same histograms for HF-, which is symmetric with HF+ but does not contain any new PMTs, are also presented.

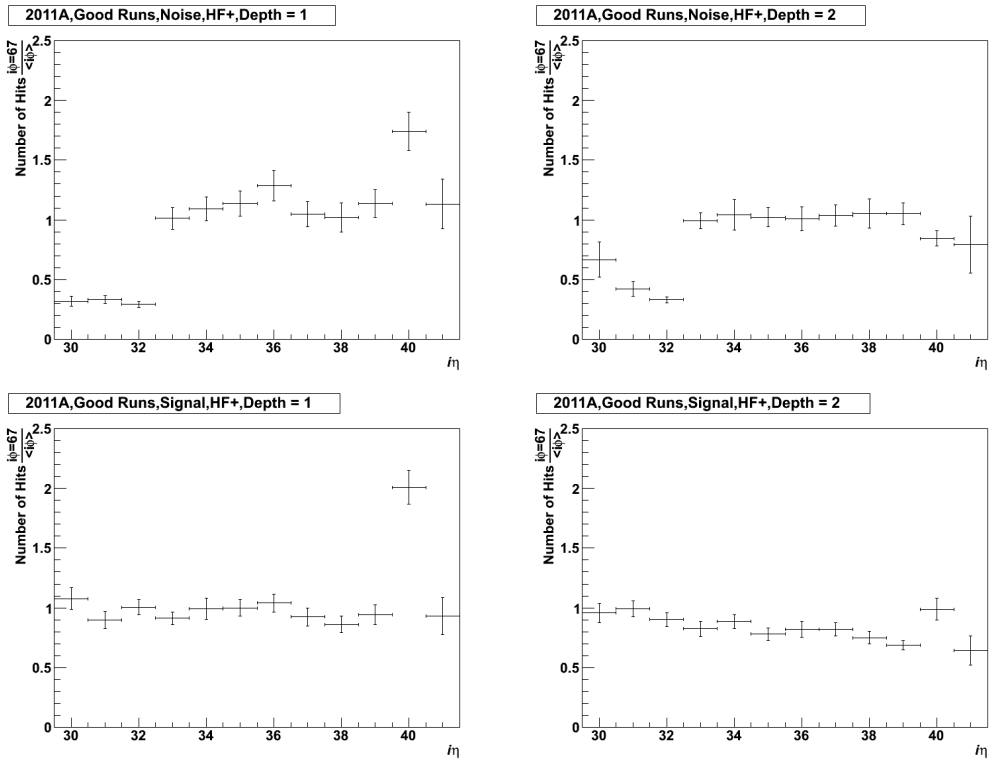

Figure 6.15. η distribution of $\phi = 67$, HF+ hits, divided by the η distribution averaged over all other ϕ values (2011A dataset). The new PMTs at $\eta = 30, 31, 32$ recorded significantly less noise compared to the PMTs at other η values. Removal of bad runs reveals a result similar to that of the 2011B dataset. Again the bottom row is for the signal case.

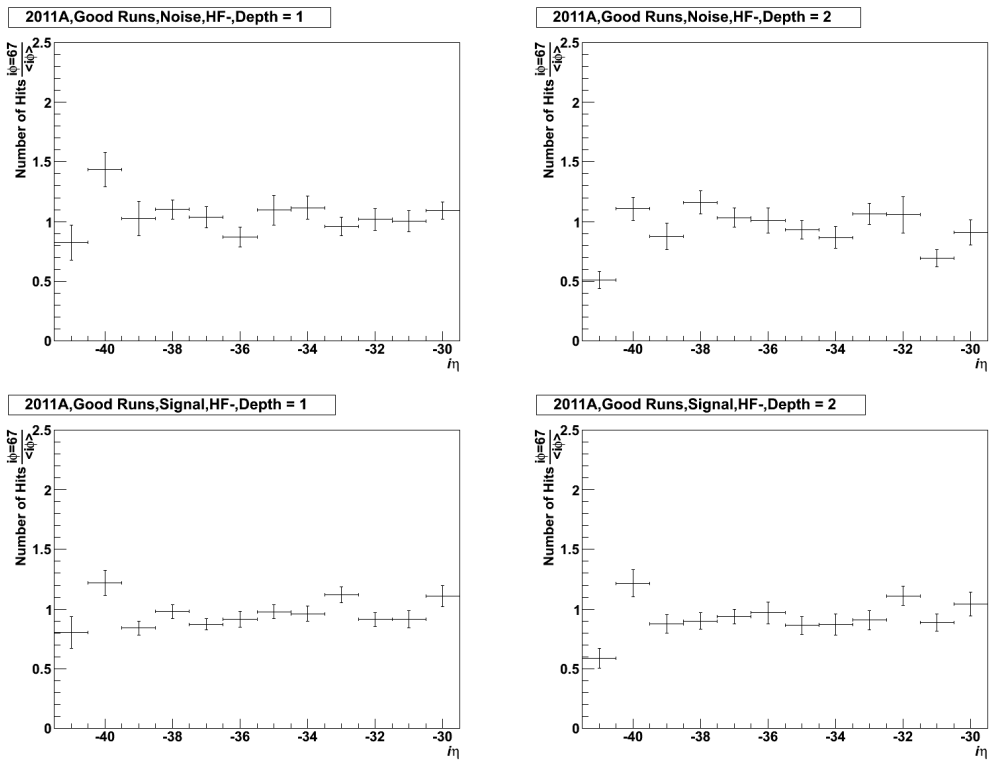

Figure 6.16. For comparison, η distribution of $\phi = 67$, HF- hits, divided by the η distribution averaged over all other ϕ values (2011A dataset) are given. The distribution is mostly flat, except for statistical fluctuations, since all η channels pertain to the same PMT type. Again the bottom row is for the signal case.

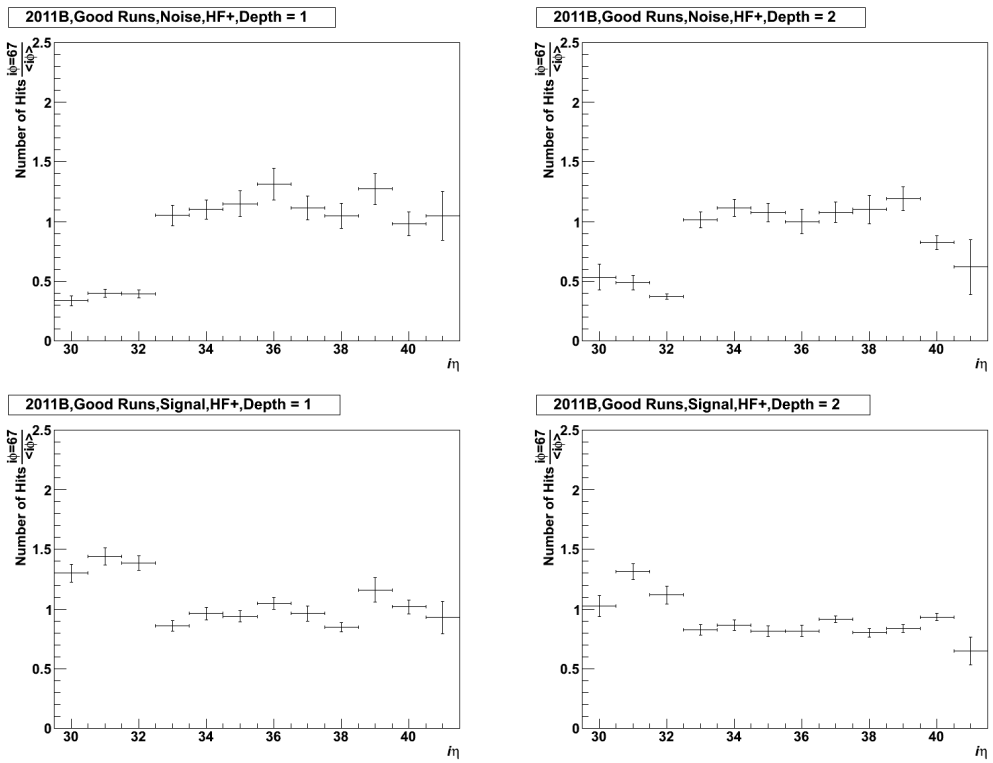

Figure 6.17. η distribution of $\phi = 67$, HF+ hits, divided by the η distribution averaged over all other ϕ values (2011B dataset). The new PMTs at $\eta = 30, 31, 32$ recorded significantly less noise compared to the PMTs at other η values. The signal rate is flat as expected. Again the bottom row is for the signal case.

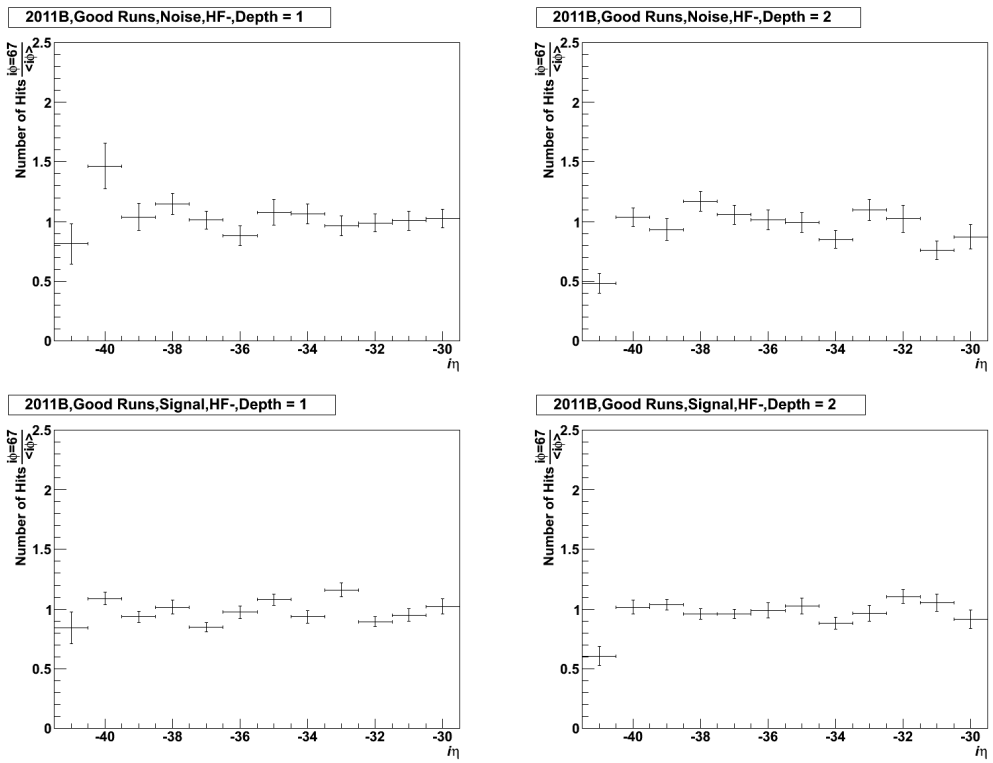

Figure 6.18. For comparison, η distribution of $\phi = 67$, HF- hits, divided by the η distribution averaged over all other ϕ values (2011B dataset) are given. The distribution is mostly flat, except for statistical fluctuations, since all η channels pertain to the same PMT type. Again the bottom row is for the signal case.

7. CONCLUSION

The purpose of this study was to compare the performance of the new quad-anode PMTs to the old single-anode PMTs, with respect to their window hit response. PMT window hits are an important problem in the HF. They are difficult to identify at trigger level and cause problems on account of their high energy deposition, since they mimic discovery events. The new quad-anode PMTs offer a simple yet powerful method for window hit rejection; absence of signal in any quadrant implies a window hit. However, setting up the HF calorimeter so that all four quadrants are readout separately is very costly, and therefore not feasible, it is important that the new PMTs perform well, even without resorting to individual quadrant information.

The method employed in this thesis to identify window events was pulseshape analysis. 2011 Jet data (2011A and 2011B) were analyzed using ROOT. The final results, with the HF+ and HF- histograms superimposed are presented below (Figures 7.1 and 7.2).

The average noise rate is significantly lower for the new PMTs; below 0.5 for long fibers (Depth = 1), and close to 0.5 for short fibers (Depth = 2). Comparison of the average noise rates of the PMTs at $i\eta = 30, 31, 32$ at HF+, which uses quad-anode PMTs, and HF-, which uses the old single-anode PMTs, corroborates the finding that the drop in $i\eta = 30, 31, 32$ is not statistical and due to the superior performance of the quad-anode PMTs. Since all four channels in each PMT are combined and readout as one output, the reduction of noise rate is due to the thinner windows which decrease the Čerenkov light from muon hits. The noise rate is lower despite the higher quantum efficiency of the quad-anode PMT.

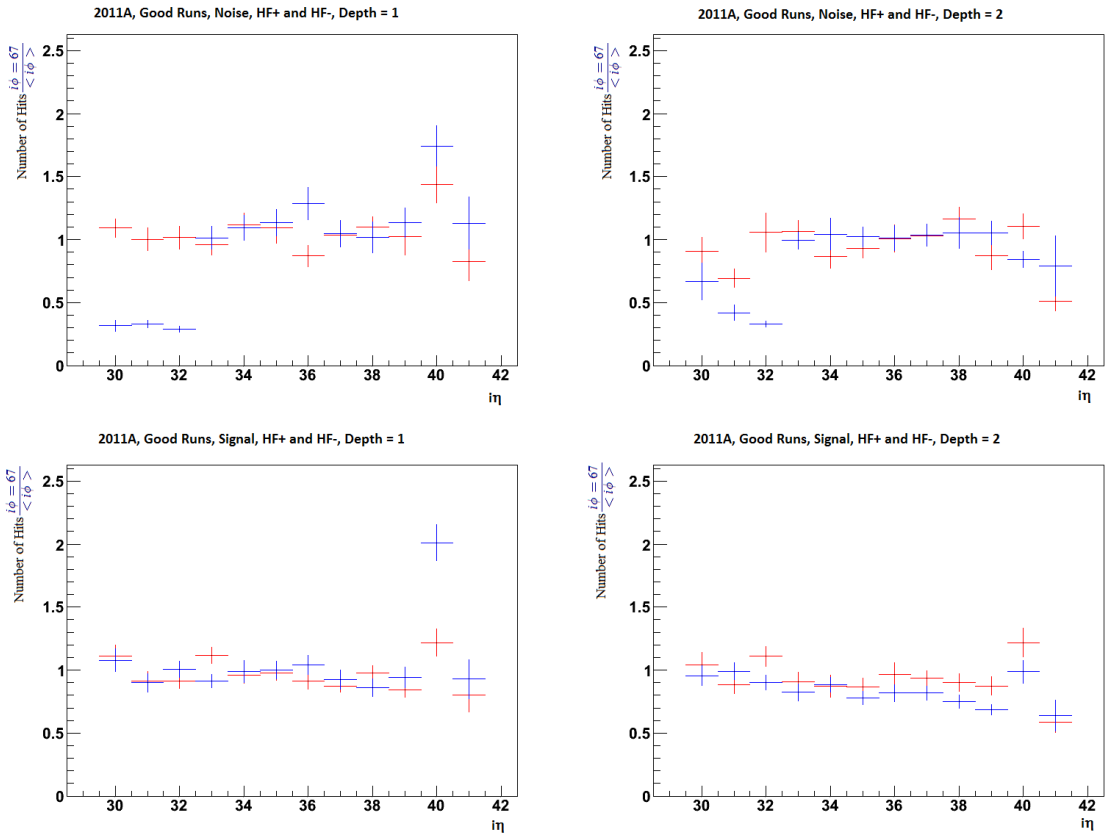

Figure 7.1. Results for the 2011A dataset, with HF+ (blue) and HF- histograms (red) superimposed. (Top histograms are for the noise and the bottom for the signal.)

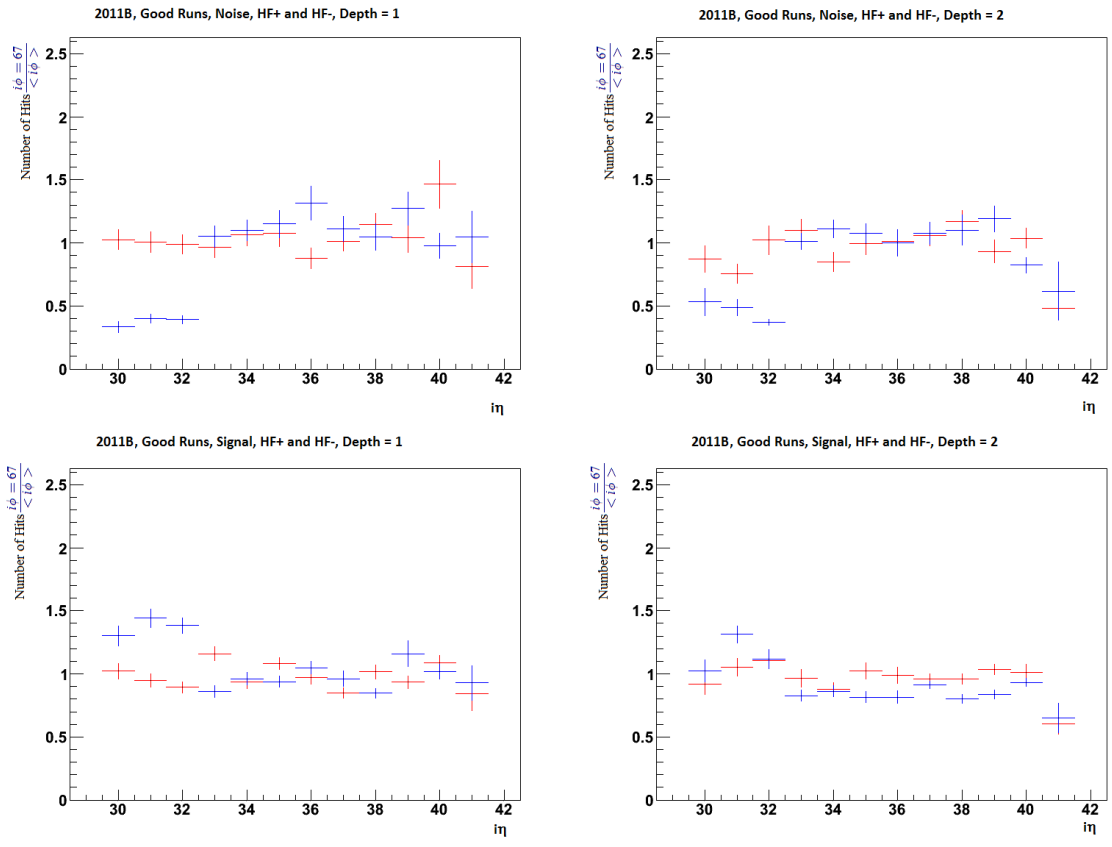

Figure 7.2. Results for the 2011B dataset, with HF+ (blue) and HF- histograms (red) superimposed. (Top histograms are for the noise and the bottom for the signal.)

The 2013 upgrade will see the old Hamamatsu R7525HA single-anode PMTs replaced by the quad-anode Hamamatsu R7600U-200-M4 PMTs. Combined with multi channel readout (one readout per two PMT quadrants) after 2015, the superior muon noise performance of the new PMTs will help alleviate the impact of window hits on physics analysis. Efforts by the researcher to extend the analysis to 2013 data is under way.

REFERENCES

1. Mans, J., *CMS Technical Design Report for the Phase 1 Upgrade of the Hadron Calorimeter*, Tech. Rep. CMS-TDR-10, CMS Collaboration, CERN, Geneva, 2012.

2. Evans, L. and P. Bryant, "LHC Machine", *Journal of Instrumentation*, Vol. 3, No. 8, p. S08001, 2008.

3. *CERN LHC: The Guide. FAQ. Frequently Asked Questions*, CERN, Geneva, 2006.

4. Rumolo, G., G. Iadarola, O. Dominguez, G. Arduini, H. Bartosik, S. Claudet, J. Esteban-Müller, F. Roncarolo, E. Shaposhnikova and L. Tavian, *LHC Experience with Different Bunch Spacings in 2011 (25, 50 and 75ns)*, 2012, Proceedings of Chamonix 2012 Workshop on LHC Performance.

5. Chatrchyan, S., V. Khachatryan, A. M. Sirunyan, A. Tumasyan, W. Adam, E. Aguilo, T. Bergauer, M. Dragicevic, J. Erö, C. Fabjan *et al.*, "Search for the standard model Higgs boson produced in association with W and Z bosons in pp collisions at $\sqrt{s}$=7 TeV", *J. High Energy Phys.*, 2012.

6. Martin, B. and G. Shaw, *Particle Physics*, Manchester Physics Series, Wiley, Wiltshire UK, 2013.

7. Bayatian, G. L., S. Chatrchyan, G. Hmayakyan, A. M. Sirunyan, W. Adam, T. Bergauer, M. Dragicevic, J. Ero, M. Friedl, R. Fruehwirth *et al.*, *CMS Physics: Technical Design Report Volume 1: Detector Performance and Software*, CERN, Geneva, 2006.

8. *The CMS Magnet Project: Technical Design Report*, CERN, Geneva, 1997.

9. Fabjan, C. W. and F. Gianotti, "Calorimetry for particle physics", *Rev. Mod. Phys.*, Vol. 75, pp. 1243–1286, 2003.

10. Leo, W. R., *Techniques for Nuclear and Particle Physics Experiments: A How-to Approach, 2nd Ed.*, Springer, New York, 1994.

11. Gavrilov, V. and M. Danilov, "Cherenkov Quartz Calorimeter", *Physics of Atomic Nuclei*, Vol. 67, No. 7, pp. 1390–1397, 2004.

12. Abdullin, S., V. Abramov, B. Acharya, M. Adams, N. Akchurin, U. Akgun, E. Anderson, G. Antchev, M. Arcidy, S. Ayan *et al.*, "Design, performance, and calibration of CMS forward calorimeter wedges", *The European Physical Journal C*, Vol. 53, No. 1, pp. 139–166, 2008.

13. *The CMS Hadron Calorimeter Project: Technical Design Report*, CERN, Geneva, 1997.

14. Wikipedia, "Photomultiplier — Wikipedia, The Free Encyclopedia", , 2013, `http://en.wikipedia.org/w/index.php?title=Photomultiplier&oldid=555114846`, [Online; accessed May-2013].

15. Akgun, U., A. Ayan, G. Aydin, F. Duru, J. Olson and Y. Onel, *Afterpulse Studies for HF Calorimeter PMTs*, Tech. Rep. CMS IN 2004/034, 2004.

16. Moeller, A., Y. Onel and T. Yetkin, *Analysis of Abnormally High Energy Events in CMS Forward Calorimeters*, Tech. Rep. CMS IN 2008/014, 2008.

17. Akgun, U., A. Albayrak, B. Bilki, W. Clarida, F. Duru, A. Moeller, Y. Onel, F. Ozok, S. Sen and T. Yetkin, *A Novel Method to Eliminate Muon Events on HF PMT Windows*, Tech. Rep. CMS DN 2009/014, 2009.